

Multi-year Arctic Sea Ice Classification

Using QuikSCAT

Aaron M. Swan

A thesis submitted to the faculty of
Brigham Young University
in partial fulfillment of the requirements for the degree of

Master of Science

David G. Long, Chair
Richard W. Christiansen
Brian A. Mazzeo

Department of Electrical and Computer Engineering

Brigham Young University

August 2011

Copyright © 2011 Aaron M. Swan

All Rights Reserved

ABSTRACT

Multi-year Arctic Sea Ice Classification

Using QuikSCAT

Aaron M. Swan

Department of Electrical and Computer Engineering

Master of Science

Long term trends in Arctic sea ice are of particular interest with regard to global temperature, climate change, and industry. This thesis uses microwave scatterometer data from QuikSCAT and radiometer data to analyze intra- and interannual trends in first-year and multi-year Arctic sea ice. It develops a sea ice type classification method. The backscatter of first-year and multi-year sea ice are clearly identifiable and are observed to vary seasonally. Using an average of the annual backscatter trends obtained from QuikSCAT, a classification of multi-year ice is obtained which is dependent on the day of the year (DOY). Validation of the classification method is done using regional ice charts from the Canadian Ice Service. Differences in ice classification are found to be less than 6% during the winters of 06-07, 07-08, and the end of 2008. Anomalies in the distribution of sea ice backscatter from year to year suggest a reduction in multi-year ice cover between 2003 and 2009 and an approximately equivalent increase in first-year ice cover.

Keywords: QuikSCAT, sea ice classification, Arctic, microwave remote sensing

ACKNOWLEDGMENTS

To my wife, Krystal, I give my most sincere thanks for her patience and sacrifice as I pursued this endeavor. I am grateful to her and our children, Lincoln, Ivan, and Adelia (and any others that might come along) for giving me purpose in my education.

My sincere gratitude to my advisor Dr. David G. Long for his expert guidance, and counsel. His patience in allowing me to grasp and pursue each problem as my research developed will always be a benefit to me.

I am grateful to my parents who instilled in me a desire to learn and gave me the tools to take my education into my own hands. They made many sacrifices to educate me and my siblings. Their advice (which at times has simply been to go to bed while working on a late night project) has served me well.

And many thanks to my friends in the Microwave Earth Remote Sensing Lab for their support and input in compiling this work.

Table of Contents

List of Tables	xi
List of Figures	xvii
1 Introduction	1
1.1 Remote Sensing of Sea Ice	1
1.2 Research Problem Description	3
1.3 Thesis Statement	5
1.4 Research Contributions	6
1.5 Thesis Organization	6
2 Background	9
2.1 Sea Ice	9
2.2 Passive Microwave Sensing of Sea Ice	11
2.2.1 Brightness Temperature	11
2.2.2 Satellite Radiometers	12
2.3 Active Microwave Sensing of Sea Ice	13
2.3.1 Normalized Radar Cross Section	13
2.3.2 Satellite Scatterometers	14
2.4 Orbital Sampling	16
2.5 Review of the NASA Team Algorithm	16

3	Method of Sea Ice Investigation	21
3.1	Data Preparation	21
3.2	Joint Analysis of Passive and Active Microwave Data	22
3.2.1	Ratios of Brightness Temperature	22
3.2.2	Analysis with QuikSCAT	27
3.3	Variability in Sea Ice Signatures	28
3.3.1	Histogram Estimation	30
3.3.2	Multi-dimensional Clustering Algorithm	34
4	Intra- and Interannual Sea Ice Trends	43
4.1	Isolating High Sea Ice Concentrations	43
4.2	Temporal Trends Observed in QuikSCAT Measurements	46
4.2.1	Trends in First-Year Ice	47
4.2.2	Trends in Multi-Year Ice	49
4.2.3	Interannual Trends in Sea Ice Coverage	53
4.3	Conclusion	54
5	Multi-Year Ice Classification and Validation	57
5.1	Multi-Year Ice Classification	57
5.2	Validation	59
5.3	Discussion of Results	62
5.4	Conclusion	62
6	Conclusion	67
6.1	Contributions	68
6.1.1	Automated Data Clustering	68

6.1.2	New Classification Method	68
6.1.3	Documented Sea Ice Change	68
6.2	Future Research	69
6.2.1	Backscatter Derived Sea Ice Age	69
6.2.2	Optimal Sea Ice Classification	69
6.2.3	Joint Active and Passive Microwave Sea Ice Classification	69
6.2.4	Active Sea Ice Classification Using C-Band	69
6.2.5	Additional Validation	70
	Bibliography	71

List of Tables

2.1 Northern Hemisphere tie-points for the NT algorithm	19
---	----

List of Figures

1.1	Location map for the north pole region.	2
2.1	Plate (dendrite) and groove structure of columnar sea ice crystals. Brine is trapped between plates. Adapted from [3].	10
2.2	Backscatter interactions for MY ice, FY ice, and open water. After [20].	14
2.3	Scanning Configuration of SeaWinds. After [29].	15
3.1	Arctic no-data and land mask in polar stereographic projection. The land mask is dilated using the shown structuring element to remove measurements with coastal effects.	23
3.2	An example of binary dilation. (a) shows a sample binary mask (white), (b) shows pixels dilated by the structuring element (gray), and (c) shows the new mask.	23
3.3	Typical histograms of AMSR-E V and H 18.7 GHz measurements during the winter. Each histogram has three modes representing open water, MY ice, and FY ice from left to right. The approximate distance between modes of open water and MY ice is shown for each histogram. Data is taken from DOY 15, 2003.	25
3.4	Calculated emissivity for horizontal (solid line) and vertical (dashed line) polarizations for $\mu_r = 1$ and $\epsilon_r = 54.4 - 36.8j$. These are typical values for sea water at 20° C with 36‰ salinity [27]. The solid red line shows the incidence angle used by AMSR-E.	26
3.5	Typical histograms of AMSR-E V 18.7 GHz and V 36.5 GHz measurements over ice during the winter. Each histogram is bimodal where the left mode represents MY ice and the right mode represents FY ice. The approximate distance between modes is shown for each histogram. Data is taken from DOY 15, 2003.	27

3.6	A joint histogram shows the relationship between R_P and R_G with marginal histograms shown to the left and bottom. The joint histogram has been log-height scaled to show more detail. Data is taken from DOY 15, 2003.	28
3.7	SIR images of both (a) QuikSCAT VV and (b) AMSR-E gradient ratio (R_G) show clear separations in FY and MY ice. (c) A joint histogram shows the relationship between these two data sets for measurements over ice with marginal histograms shown to the left and below. The line shows an approximate separation of FY and MY ice. The joint histogram has been log-height scaled to show more detail. Ocean has been removed using a mask. Data is taken from DOY 15, 2003.	29
3.8	Joint histograms of R_P and R_G for (a) DOY 336, 2004 and (b) DOY 32, 2005 with marginal histograms shown to the left and bottom. Approximate modes are annotated by solid squares in (a) and solid circles in (b). These annotations are replicated as dashed shapes in each image for comparison. The joint histograms have been log-height scaled to show more detail.	31
3.9	Histograms of (a) AMSR-E $R_P(18.7)$ and (b) QuikSCAT VV measurements. Each histogram is bimodally distributed with maximums and minimum (between maximums) marked. Data is taken from DOY 32, 2003.	32
3.10	Rough classifications for OW, FY ice, and MY ice over the Arctic for DOY 32, 2003.	32
3.11	Restricted distribution of $R_G(36.5, 18.7)$ under the rough (a) open water, (b) FY ice, and (c) MY ice classifications. The dashed lines represent the restriction which is based on half the height of the mode. Data is taken from DOY 32, 2003.	33
3.12	Final classifications for OW, FY ice, and MY ice for DOY 32, 2003.	34
3.13	Histogram of points on a line demonstrating the difficulty of detecting clusters with a threshold.	35
3.14	OPTICS Definitions: (a) P is in the ϵ -Neighborhood of Q. (b) The center point is a core object ($MinPnts = 4$). (c) Points inside the circle (such as P) are directly density-reachable from Q. (d) P is density reachable from Q. See text.	37
3.15	OPTICS Definitions: (a) P is density connected to Q (b) Solid points belong to clusters. Other points are noise. See text.	37

3.16	OPTICS Definitions: Arrows represent reachability distance. Point A is inside the core-distance radius. Point B sets the core-distance for $MinPnts = 4$. Point C is outside the core, but inside the generating distance. Point D is outside the generating distance. It has UNDEFINED reachability-distance. See text.	38
3.17	The OPTICS Algorithm	39
3.18	Reachability plot example for three random clusters. The relationship between clusters and valleys is indicated by arrows. MinPnts is set to 100.	40
3.19	Reachability distance plot generated by the OPTICS algorithm for a two-dimensional set consisting of AMSR-E R_G and QuikSCAT VV. The red dashed lines terminated by triangles indicate sets of points within a cluster. This plot only represents 1 out of every 100 points to reduce excessive detection of clusters and increase processing speed. Data is taken from DOY 15, 2003. . .	41
3.20	Clusters determined using the OPTICS algorithm are mapped over AMSR-E R_G . Clusters are shown in color. (a) is an all-inclusive cluster, (b) represents open water, (c) represents FY ice, and (d) represents MY ice. Data is taken from DOY 15, 2003.	42
4.1	Typical joint histograms of AMSR-E 6 GHz V brightness temperatures and ice concentrations from the NASA Team algorithm for selected days of the year (DOY) in 2004. Histogram bins have been log height scaled. The horizontal line represents a threshold at 220 K.	44
4.2	AMSR-E 6 GHz V brightness temperatures (K) over the Arctic on DOY 32, 2005 (land has been excluded). The ocean and ice measure approximately 160 K and 250 K respectively.	45
4.3	A daily time series of histograms of AMSR-E 6 GHz V brightness temperatures over the Arctic during 2004. Histograms are normalized and exclude measurements over land. The dashed line represents a threshold separating modes representative of ocean and ice. The summer melt period is indicated by a solid line.	46
4.4	A typical SIR image of QuikSCAT VV (σ^0 in dB). The ocean has been masked by applying a threshold to collocated AMSR-E brightness temperatures. (DOY 20, 2004).	47
4.5	Temporal series of histograms of QuikSCAT VV backscatter over sea ice during the 06-07 winter.	48

4.6	Seasonal trends in backscatter over FY and MY ice. (a) shows a time series of histograms of backscatter over Arctic sea ice for the winter of 04-05. (b) shows approximate ranges of backscatter for FY and MY ice for each year between 2003 and 2009. The range of backscatter for each ice type appears to be seasonally dependent.	50
4.7	Time series of histograms of QuikSCAT VV measurements over sea ice during the 07-08 winter. The gray scale emphasizes that multiple modes are present in the typical range for MY ice.	51
4.8	Typical results for collocated σ^0 VV measurements and CRREL buoys (above), and buoy positions (below).	53
4.9	(a) Temporal series of histograms of QuikSCAT VV measurements over sea ice, and (b) the total area of ice above the $A_{6,V}$ 220 K threshold for each day.	55
4.10	A plot of backscatter versus time for two different winters. The winter of 02-03 is shown on the left and 08-09 on the right. The FY ice mode is marked by a solid line, and the MY ice mode by a dashed line for each winter. Note that MY ice distributions are brighter during the winter of 02-03 and FY ice distributions are brighter during the winter of 08-09.	56
4.11	Selected QuikSCAT VV (σ^0 in dB) images showing trend in decreasing MY ice from 2003-2009. Images from left to right represent DOY 32, in 2003, 2006, and 2009. Land is shown as black, and ocean is dark blue. Brighter colors correspond to increased backscatter where FY is approximately below -15 dB and MY is above.	56
5.1	(a) An annual time series of daily histograms averaged over 7 years (2003 to 2009). The dashed box represents a subset shown in (b). (b) The classification threshold on QuikSCAT backscatter distributions. Shown are bounds set to select the minimum (dashed straight lines), the minimum found for each day of the year (+), and a curve fitted to the results (solid curve) with 95% confidence intervals (dashed curves).	58
5.2	Canadian Ice Service Chart Regions (Modified from [46]).	60
5.3	Collocated CIS Western Arctic ice chart and QuikSCAT SIR image on DOY 42, 2008. Land is black. (a) shows the percent ice concentration for the highest ice stage concentrations for each ice chart subregion. (b) shows ice stage concentrations above 70% grouped as FY or MY ice overlaid on a QuikSCAT SIR image (σ^0 in dB).	61

5.4	Classification error of QuikSCAT-derived FY/MY ice using CIS ice charts. The error represents the percentage of ice cover misclassified using QuikSCAT σ^0 for the (a) Western Arctic and (b) Eastern Arctic regions. The total area of ice considered (solid line) and the error for each day (stem plot) are shown.	63
5.5	Ice classification using QuikSCAT for DOY 32, 2003 through 2009. Note the trend in decreasing spatial coverage of MY sea ice.	64

Chapter 1

Introduction

Satellite remote sensing of the polar ice caps is a primary means of monitoring sea ice coverage today [1]. Many studies have been devoted to understanding sea ice dynamics and estimating and validating sea ice concentration and classification methods.

Sea ice is dynamic both intra- and interannually. In 2010, Arctic sea ice extent, which includes sea ice concentrations above 15 percent, fluctuated between 15.25 and 4.6 million square kilometers [2]. Each winter, Arctic sea ice fills the Arctic basin and commonly extends through the Bering and Fram straits shown in Figure 1.1. The high albedo (or ratio of reflected to incident light) and insulating properties of sea ice make it climatically influential. Its presence insulates warm ocean waters from much colder atmospheric temperatures, while its surface cools the earth by reflecting sunlight. Sea ice is also climatically influenced, as its rate of growth and melt depend on atmospheric conditions as well as ocean conditions, including temperature and the direction and magnitude of ocean currents under the ice [3]. Changes in the Arctic ice cover influence shipping navigation routes, the exploration of untapped mineral and oil reserves, and unique ecosystems above and below the ice [4]. The coverage of perennial or multi-year (MY) ice is of particular interest due to its greater thickness and higher albedo over seasonal or first-year (FY) ice. It contributes more stability to the ice cover and poses more danger to sea vessels than FY ice.

1.1 Remote Sensing of Sea Ice

In order to characterize changes in sea ice, a wide variety of tools are commonly used. These include observations from ships, buoys, aircraft, and satellites. Each tool has advantages and disadvantages. Ships provide direct access to the ice, allowing researchers to make measurements directly on or with close proximity to the ice. Icebreakers, which

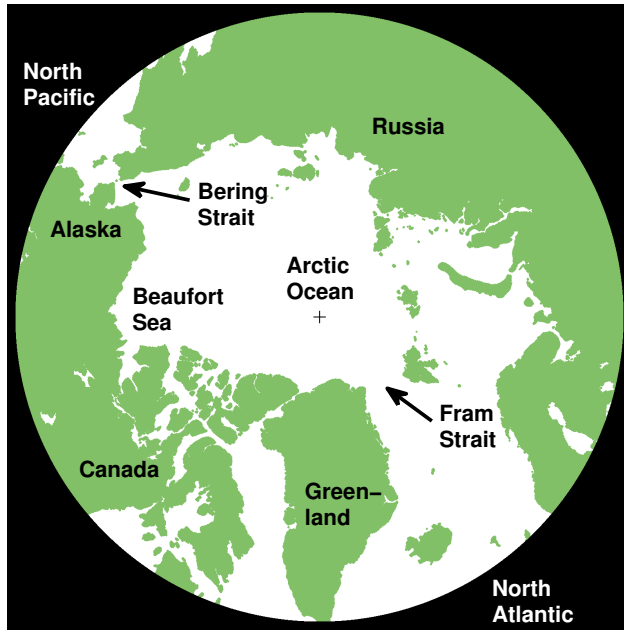


Figure 1.1: Location map for the north pole region.

can generally travel through FY or thin MY ice, provide valuable information about ice thickness, composition, and age, but are limited in spatial and temporal coverage. Buoys can continuously monitor an ice floe for multiple years. They provide a unique perspective by monitoring changes above and below the ice, but are only sparsely deployed. While there is a significant shortage of spatial coverage, buoys move with the ice, providing historical reference points which have been used to reconstruct Arctic sea ice motion and age [5]. Aircraft can provide localized spatial coverage over large areas of ice and can be configured with several remote sensing devices such as high resolution cameras, synthetic aperture radars (SAR), radiometers, scatterometers, and altimeters. Although greater spatial coverage is achieved, it comes at a loss of direct contact with the ice. While still remote, satellite-borne sensors provide frequent and consistent data samples, with broader, more complete, coverage than aircraft. Depending on orbital parameters, these sensors are capable of providing complete daily coverage of the poles. Some drawbacks of satellite-borne sensors include atmospheric influences and limited resolution. Satellites are also costly to produce and operate.

Optical remote sensing of the Arctic can be difficult because the Arctic is often shrouded by cloud cover and is dark several months out of the year. Satellite based optical sensors provide high resolution imagery, but are only useful for sea ice monitoring under clear-sky, lighted conditions. Microwave sensors provide two major advantages over optical sensors: depending on the observation frequency, the atmosphere is relatively transparent to microwaves, allowing them to pass through clouds nearly unaffected; and microwave sensors do not rely on the sun for illumination.

There are two types of microwave sensors: passive and active. Passive microwave sensors (radiometers) “listen” to radiation that is naturally emitted by all materials above absolute zero. They measure brightness temperature, which is related to microwave energy. Brightness temperature is the product of the physical temperature and emissivity of a material, under some simplifying assumptions. Active microwave sensors (scatterometers) provide their own source of illumination by transmitting a pulse of microwave energy. They measure the backscattered radiation, which is a function of the reflecting material’s permittivity and physical roughness. This measured radiation (normalized by the area under illumination) is referred to as the normalized backscatter cross section or σ^0 . Satellite-borne microwave sensors, passive and active, have been used in various studies to estimate sea ice concentration and extent [6, 7, 8, 9, 10, 11] as well as to classify sea ice as FY or MY ice [12, 13, 14].

1.2 Research Problem Description

In the past decade, significant changes have occurred in Arctic sea ice. Kwok *et al.* [15] report findings of interannual MY sea ice loss through a study of ice thickness. In their study, a five year period from 2003 to 2008 was investigated during which *ice draft* profiles were obtained from a submarine cruise and moorings in the Chukchi and Beaufort seas. Ice draft refers to the portion of sea ice below the surface of the water. Additional estimates of the ice draft were made using a laser altimeter aboard the Ice, Cloud, and Land Elevation Satellite (ICESat) to retrieve elevation data over the Arctic ocean. The study concluded that in the 4 years following 2005, there was a net loss in MY sea ice volume of 6300 km³, which corresponds to a 42% decrease.

These changes, and the potential impact of Arctic sea ice on climate, ecology, and industry, necessitate the improvement and development of accurate methods and models to monitor sea ice. In terms of sea ice classification, microwave backscatter has been found to produce more temporally stable results than microwave brightness temperature [12]. Sea ice classification algorithms using passive microwave data have been shown to be unreliable in multiple studies [7, 16, 17].

A 2004 study conducted by Kwok [14] compares three data sources: scatterometer measurements from QuikSCAT; ice motion charts, derived from passive microwave measurements; and synthetic aperture radar (SAR) imagery and MY ice coverage estimates from RADARSAT. These were used in an effort to classify and explain variations in MY ice coverage. For this study, a seasonal ice zone (SIZ) and perennial ice zone (PIZ) are defined, where the SIZ consists of first-year and younger ice and the PIZ consists of second year and older ice [18]. A persistent contrast in backscatter of 4 to 7 dB is found to exist between the SIZ and PIZ. The efficacy of using a fixed threshold to classify these ice types depends on the stability of backscatter over sea ice and on the variability of the sensor. Observations of backscatter over sea ice indicate that while significant variability exists during fall and into November, the microwave signatures of the SIZ and PIZ stabilize by December. Assuming that sea ice backscatter remains stable during the winter, attention is turned to sensor variability. To verify that there is little variability in the calibration of the sensor, backscatter measurements are obtained over the dry snow zone in Greenland. The resulting variability is less than 0.1 dB over a period of 4 years. Given the stability of backscatter during the winter and the accuracy of the sensor, an optimal classification threshold of -14.5 dB is found by visually comparing high resolution RADARSAT SAR imagery with thresholded QuikSCAT backscatter measurements.

This sea ice classification method, as well as the NASA Team sea ice concentration algorithm, rely on fixed reference values. These values are broadly applied during the winter season without consideration for seasonal changes. Since the sea ice scattering and emission characteristics vary intra-seasonally, it is not clear that using fixed reference values is appropriate.

1.3 Thesis Statement

The purpose of this thesis is to develop a new method for the classification of seasonal and perennial sea ice using a Ku-band scatterometer. To this end, multiple approaches are used to investigate the microwave characteristics of sea ice. Passive and active microwave data from different sensors are analyzed for different polarizations, frequencies, and incidence angles.

This thesis is divided into two parts. In the first part, sea ice type and concentration are considered. Two different methods are developed to automatically derive probability distributions representative of open water, FY ice, and MY ice on a daily basis. The first method relies on one-dimensional histograms of arithmetic combinations of microwave data, while the second employs an automatic clustering algorithm which reduces the multiple dimensions of available data to a one-dimensional problem. Both methods incorporate active and passive microwave data.

In the second part, attention is focused on sea ice classification using only active microwave measurements. Using a simple mask to remove measurements over the ocean, I study the temporal evolution of sea ice backscatter over several winter seasons. From clearly visible trends in the distribution of sea ice backscatter, which provide insight into the backscatter signatures of aging sea ice, I derive a sea ice classification method using QuikSCAT measurements over a period of seven years. The vertically (and horizontally) polarized backscatter measured by QuikSCAT over sea ice is bimodally distributed, where the modes represent FY and MY ice. The minimum between these modes provides a threshold for the classification of sea ice. To derive this distribution (and minimum), histograms are taken from the seven year period for a given day of the year and averaged. A curve, dependent on the day of the year, is then fit to the resulting minimums to produce a classification threshold for each day of the winter. The application of this classification method independently confirms that the coverage of MY ice has reduced from year to year relative to FY ice between 2003 and 2009, as was previously reported in [15]. This thesis demonstrates the potential of scatterometry for FY and MY sea ice classification.

1.4 Research Contributions

The research presented in this thesis contributes to the body of published work on the remote sensing of Arctic sea ice by documenting several observations with respect to intra- and interannual sea ice backscatter characteristics, and by documenting the development and validation of a seasonal sea ice classification model. These contributions include (1) an analysis of temporal (seasonal) changes in Ku-band backscatter of FY and MY sea ice, (2) the spatial and temporal tracking and analysis of backscatter over MY ice, (3) the observation of a multi-year trend in the decrease of MY Arctic sea ice coverage, and (4) a new MY Arctic sea ice classification algorithm. The classification algorithm independently confirms that the coverage of MY ice has reduced from year to year relative to FY ice between 2003 and 2009. Essential results of this thesis are contained in [19], which has been submitted for publication.

1.5 Thesis Organization

This thesis is divided into two major topics: an analysis of intra- and interannual sea ice trends, and the classification and validation of a new MY sea ice classification algorithm. A brief description of each chapter is given below:

Chapter 2 begins with a discussion of the importance and formation of Arctic sea ice. The theory and application of microwave sensing of sea ice are then reviewed with a brief history of satellite radiometers and scatterometers. It continues with an overview of orbital sampling and discusses some techniques used in the formation of satellite imagery, and concludes with a review of the NASA Team algorithm.

Chapter 3 is an overview of initial research performed in the investigation of passive and active microwave measurements over the Arctic. Multiple approaches to sea ice characterization are tested and reviewed including the evaluation of previously published methods.

Chapter 4 outlines intra- and interannual trends in sea ice backscatter. Initially, a method of separating sea ice and ocean is presented, which uses AMSR-E brightness temperature measurements. The backscatter over sea ice is then discussed with a focus on

temporally dependent trends in the distribution of backscatter. The chapter concludes with evidence of a multi-year trend in the decrease of MY ice.

Chapter 5 presents a new algorithm for the classification of MY sea ice. A minimum is observed to exist between FY and MY ice in the daily distribution of sea ice backscatter measurements. Taken over the course of winter, these minimums form a smooth temporal curve to which a polynomial is fit. This fit represents a classification threshold between FY and MY ice types, dependent on the day of the year. Results are validated using ice charts compiled by the Canadian Ice Service (CIS).

Chapter 6 concludes this thesis with a summary of the research performed. Contributions to the field of remote sensing are given followed by several paths where by future work might be pursued.

Chapter 2

Background

Microwave remote sensing has been employed to monitor the earth for nearly five decades. The polar ice caps have been monitored by satellite radars and radiometers almost continuously for more than three decades producing a vast accumulation of scientific research on the active and passive microwave characteristics of sea ice. This chapter begins with a discussion of the importance and formation of sea ice. The theory and application of microwave sensing of sea ice are reviewed next with a brief history of satellite radiometers and scatterometers. This chapter concludes with a discussion of image formation from orbital samples and a review of the National Aeronautics and Space Administration (NASA) Team (NT) sea ice concentration algorithm.

2.1 Sea Ice

Understanding the formation, composition, and dynamics of sea ice is critical to interpreting microwave measurements. When the ocean surface is sufficiently cooled, ice formation begins with small needles and platelets called *frazil*. Unconsolidated frazil is commonly referred to as *grease ice* due to its appearance. Under calm water conditions, frazil consolidates to form an ice cover up to 10 cm thick called *nilas*. Under stormy conditions, it is possible for thick layers of frazil to form, or for nilas (or other ice types) to be broken in pieces and later reconsolidate. Once a layer is formed, the rate of continued ice growth under it depends on the temperature gradient of the ice. In a process known as *geometric selection*, new ice crystals forming in competing orientations are eliminated. Non-competitive growth occurs only perpendicular to the ice surface. The process of geometric selection results in a transition layer of 5 to 10 cm in thickness, which precedes the formation of vertically oriented ice crystals known as *columnar ice* extending beneath it [3].

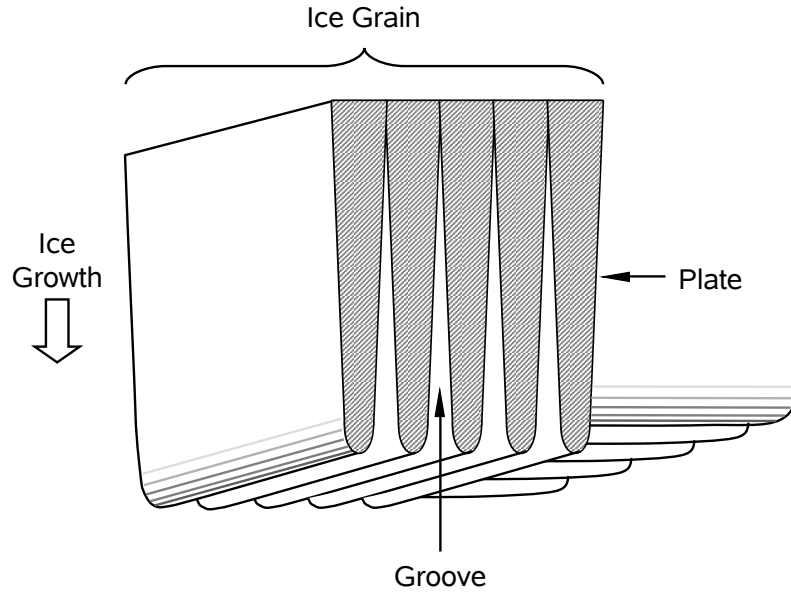


Figure 2.1: Plate (dendrite) and groove structure of columnar sea ice crystals. Brine is trapped between plates. Adapted from [3].

During the formation of sea ice, brine becomes trapped in the ice by the more rapid diffusion of heat than salt. In columnar ice, which comprises the remainder of the ice sheet (in a typical calm water scenario), each grain of ice is composed of ice plates (dendrites) and grooves where brine is trapped. This structure is illustrated in Figure 2.1. Brine drainage, which begins after ice forms, increases the porosity of sea ice and alters its microwave characteristic. The drainage is caused by an imbalance in temperature, pressure, and salinity in the ice, and continues until a stable equilibrium point is found. Ice melt and formation on the inside of a brine pocket change the salinity of the brine as well as the pressure within the pocket, which is due to the differing densities of ice and water. Increases in pressure can force brine up or down out of the brine pocket through cracks in the ice. The deformation of brine pockets causes them to merge together creating larger pockets and networks of channels in the ice.

In the change from FY to MY ice that occurs during the summer, fresh water melt on the surface of the ice drains through the network of brine channels, desalinating the upper layers of ice and enlarging the channels. As a result, sea ice near the top surface is nearly salt free and is much more porous, both of which alter its microwave scattering characteristics.

Differentiating FY and MY is important for accurately determining their respective spatial coverage. Understanding the signatures of each ice type also makes it possible to parameterize sea ice concentrations, and determine the fractional contribution of each ice type. These ice types can be distinguished by thickness, snow cover, salinity, and surface characteristics. MY ice is typically 1.5 m or thicker with a snow cover of 0.4 m, while FY is typically less than 1.5 m thick with a snow cover of 0.1 m. In some scenarios, FY ice may be thicker than MY ice. Typical sea ice salinities of FY and MY ice are 7.7‰ and 2.5‰ respectively, where ‰ means parts per thousand [20]. The surface features of FY ice tend to be sharp compared to the rounded appearance of MY ice. This is particularly true of ice ridges, which are a common feature in the shifting environment of Arctic sea ice. Ice ridges form when two ice floes are forced together. Commonly, one ice floe submerges while the other rafts on top, breaking into large ice blocks. During the summer season, sharp FY ice features, like these ridges, deform under melt and freeze cycles creating the rounded appearance of MY ice. As a result of mechanical deformations and changes in dielectric constant, MY and FY ice have different microwave scattering and emission characteristics. These are considered in the following.

2.2 Passive Microwave Sensing of Sea Ice

Microwave radiometry is used extensively in the estimation of sea ice parameters. Its usefulness arises from the unique radiation properties of snow, ice, salt, and water. This radiation, or *brightness temperature*, which is taken as noise in other applications, is carefully measured using a radiometer. The standard measure of radiation in radiometry is *brightness temperature*.

2.2.1 Brightness Temperature

All real materials, or *graybodies*, radiate energy. The amount of radiation observed from a graybody is dependent on the angle and frequency of observation. An idealized material, or *blackbody*, at temperature T and in thermal equilibrium with its surroundings, radiates at least as much energy as any other body at temperature T . By definition, blackbodies also perfectly absorb all radiation incident upon them.

To quantify the amount of energy radiated by a real material, its radiance or brightness $B(\theta, \phi)$ is defined as the radiated power per unit solid angle per unit area, where θ is the incidence angle, and ϕ is the azimuth angle. Using the Rayleigh-Jeans approximation, the brightness B_{bb} of a blackbody in the microwave region is defined as

$$B_{bb} = \frac{2k_B T}{\lambda^2} \Delta f, \quad (2.1)$$

where k_B is Boltzmann's constant, T is physical temperature, λ is the wavelength, and Δf is a narrow bandwidth. The ratio of a material's brightness to the corresponding blackbody brightness is known as the material's *emissivity*,

$$\epsilon(\theta, \phi) = \frac{B(\theta, \phi)}{B_{bb}} = \frac{T(\theta, \phi)}{T}, \quad (2.2)$$

where $T(\theta, \phi)$ or simply T_b is the blackbody equivalent radiometric brightness temperature of the material. The emissivity of a material is bounded between 0 and 1 by definition. In general, measurements of brightness temperature of the earth include natural emissions from the surface, sub-surface emissions, upwelling radiation from the atmosphere, and downwelling radiation from the atmosphere that is reflected toward the receiver. In satellite radiometry, atmospheric contributions, which are dependent on the observation frequency, must be considered [21].

2.2.2 Satellite Radiometers

Satellite radiometers have been shown to be useful in determining sea ice coverage, concentration, and type (such as FY and MY ice). The single channel Electrically Scanning Microwave Radiometer on the NIMBUS 5 satellite (ESMR-5), which operated at 19.3 GHz, demonstrated some of these applications [22]. Its single channel receiver was useful in distinguishing ice and ocean, but limited in its ability to determine ice temperature variation or ice type [6].

In 1984, the Scanning Multichannel Microwave Radiometer (SMMR) aboard the NIMBUS 7 satellite was also used to measure sea ice parameters in the NT algorithm [6, 23, 24]. SMMR had the advantage that it provided radiances at five frequencies with horizontally

(H_{pol}) and vertically (V_{pol}) polarized receivers. More recently, the NT algorithm was calibrated to use radiances measured by the Special Sensor Microwave Imager (SSM/I) instrument [25]. This data, collected under the Defense Meteorological Satellite Program (DMSP), provides dual-polarization radiances from three channels (19.35, 37.0, 85.5 GHz) and V_{pol} radiances from one additional channel (22.235 GHz).

In 2002, the Advanced Microwave Scanning Radiometer of NASA’s Earth Observing System (AMSR-E) was launched. It was developed by the National Space Development Agency of Japan (NASDA). Hardware improvements over existing spaceborne radiometers include the largest main reflector of its kind and the addition of 6.9 GHz channels. AMSR-E is currently operational and provides measurements over 6 frequencies ranging from 6.9 to 89.0 GHz. Brightness temperature measurements are taken at V_{pol} and H_{pol} at each frequency with a total of 12 channels [26]. AMSR-E is in a sun synchronous orbit and provides consistent daily coverage of the poles.

2.3 Active Microwave Sensing of Sea Ice

A microwave scatterometer is a type of radar which measures *normalized radar cross section* (σ^0) of a surface by actively illuminating the surface with microwave energy. The backscatter, or portion of the power that is reflected back toward the receiver can be related to surface roughness, structure, and other physical properties as well as dielectric constant. Backscatter is generally the result of many individual point scatterers forming a diffuse reflection, as opposed to a specular reflection from a smooth surface, as might be seen from a mirror.

2.3.1 Normalized Radar Cross Section

The power transmitted and received by a scatterometer are related by the radar equation [27],

$$P_r = \frac{P_t G^2 \lambda^2 A}{(4\pi)^3 R^4} \sigma^0, \quad (2.3)$$

where P_r is the power received, P_t is the power transmitted, G is the gain of the antenna, λ is the wavelength of the transmitted signal, A is the area of surface illumination, R is the

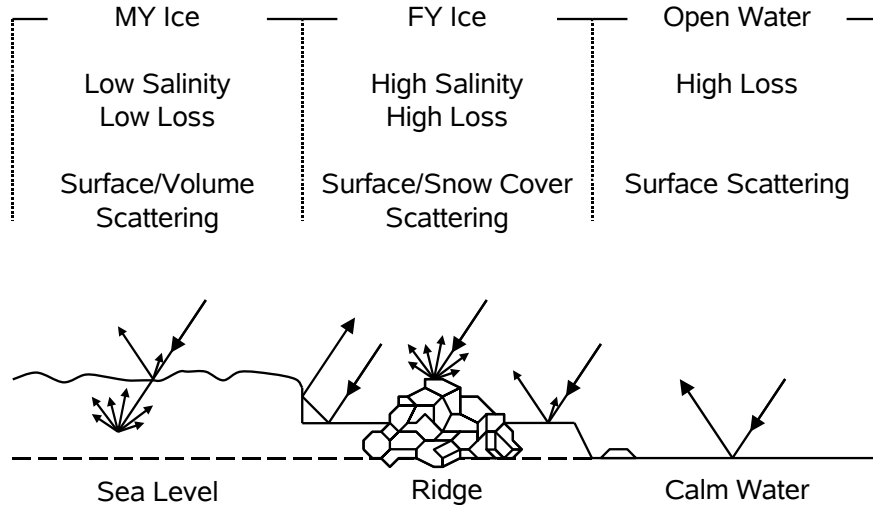


Figure 2.2: Backscatter interactions for MY ice, FY ice, and open water. After [20].

distance from the transmitter to the target (slant range), and σ^0 is the radar cross section normalized over the area of illumination.

As with radiances, the backscatter received by a scatterometer is dependent on the incidence and azimuth angles of observation (θ and ϕ). It is also dependent on the polarization and frequency of the transmitted signal. Figure 2.2 illustrates several scenarios encountered in the active sensing of sea ice. Backscatter over MY ice results from surface and volume scattering. Due to the low-loss composition of MY ice, volume scattering from gas bubbles within the ice significantly contribute to the total backscatter. Over FY ice and open water, which are both high-loss materials, backscatter is mostly due to surface roughness. From off nadir angles, very little backscatter is observed over calm ocean waters, since microwave energy is specularly reflected away from the receiver.

2.3.2 Satellite Scatterometers

Spaceborne scatterometer data has been used to investigate sea-wind interactions since the launch of the Seasat Scatterometer (SASS) by NASA in 1978. SASS, which was a Ku-band (14 GHz) fan beam scatterometer, lasted only 3 months, but provided a set of baseline measurements. SASS was followed by ERS-1 (1991) and ERS-2 (1995) developed by the European Space Agency (ESA). These scatterometers contributed C-band measurements

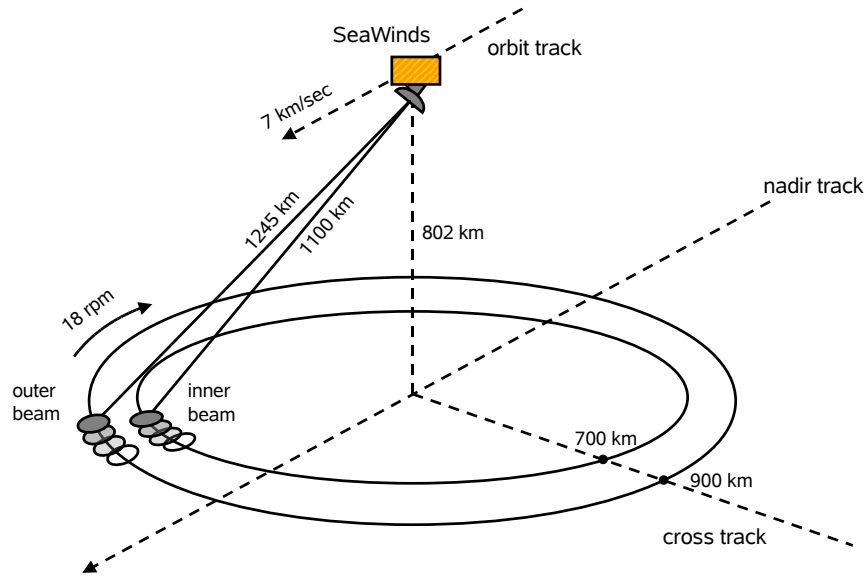


Figure 2.3: Scanning Configuration of SeaWinds. After [29].

at 5.6 GHz. In 1996, NASA launched another Ku-band fan-beam scatterometer known as the NASA Scatterometer (NSCAT), but it failed shortly after in 1997.

In response to the failure of NSCAT, the SeaWinds instrument aboard QuikSCAT was launched in 1999 [28] as a quick replacement. SeaWinds (hereafter referred to as QuikSCAT by convention) employs a rotating pencil beam antenna which transmits and receives at 13.4 GHz. The scanning configuration is shown in Figure 2.3. Measurements of normalized backscatter cross-section are collected in horizontal (HH) and vertical (VV) polarizations at incidence angles of 46° and 54.1° respectively. QuikSCAT achieved global daily coverage for 10 years producing a consistent and nearly uninterrupted data set over its period of operation. In 2009, its rotating antenna stalled, limiting further observations. Although QuikSCAT and the previous scatterometers mentioned were designed to measure wind speed and direction over the ocean, the radar backscatter measurements collected are sensitive to land, snow, water saturation, and various types of ice.

2.4 Orbital Sampling

Image formation from remotely sampled data requires consideration of the spatial sampling interval, range to the target, incidence angle, shape of the antenna footprint on the ground, and atmospheric contributions. The spatial sampling of remote sensing satellites is non-uniform in general. Measurements may be disjoint in the along track direction, and depending on the scanning geometry, may also vary in shape across the swath. Corrections to the received power can be made which account for atmospheric attenuation, range to the target, and incidence angle.

A simplistic approach to image formation is to define a spatial grid on the surface of the earth and average all of the measurements whose centers fall within a given grid element (pixel). Averaging in this manner results in a temporal/spatial resolution trade-off, where longer averages produce a higher spatial resolution of fixed features, but shorter averages reveal moving features. The effective resolution of this approach is coarser than the nominal grid spacing due to the spatial response of the antenna. Even though the center of a measurement falls within a grid element, some of the power returned to the receiver is a function of the area surrounding the grid element. The effective resolution is thus defined by the antenna footprint.

The QuikSCAT and AMSR-E data used in this paper has been processed using variations of the Scatterometer Image Reconstruction (SIR) algorithm [30, 31]. Over the poles, the SIR algorithm uses a polar stereographic grid projection. QuikSCAT SIR images are provided in log-scale at two resolutions referred to as “egg” and “slice”, where eggs and slices are standard QuikSCAT data products. Slices result from range/doppler processing on the received signal, approximately slicing the antenna footprint into several trapezoids. Eggs are an average of the 8 central slices. Although the egg SIR images used in this paper are of lower resolution than slices, they are less noisy.

2.5 Review of the NASA Team Algorithm

A long standing and often cited approach to sea ice characterization is the NT sea ice concentration algorithm [25], which is applied to radiometer data. Its popularity is likely due to its simple derivation and reasonable results. The NT algorithm derives sea ice

concentration using measurements from the spaceborne Special Sensor Microwave/Imager (SSM/I) radiometer. This data is collected under the Defense Meteorological Satellite Program (DMSP).

As discussed earlier, the brightness temperatures (T_b) measured by a radiometer are a composition of radiances from the earth, atmosphere, and space. Contributions from space and the atmosphere are noted to be very small over polar regions. The NT algorithm makes the simplifying assumption that brightness temperatures over the Arctic (excluding land) are a linear combination of fixed reference temperatures representing open water (OW), first year (FY) ice and multi-year (MY) ice. This means that measured brightness temperatures are assumed to be a function of the relative concentrations of OW, FY ice, and MY ice. The fixed reference temperatures are referred to as tie-points. While they depend on several factors including weather conditions, freezing and melting cycles, water composition, and physical temperature, they are treated as constant. Some advantages of using tie-points are (1) that they provide standard reference points for comparing ice concentrations and (2) their use has been shown to produce reasonable results. Some disadvantages are that, over the course of the year, tie-points may not always be representative of their respective materials, and that tie-points do not account for variability in ice conditions.

The NT algorithm calculates total sea ice concentration (C) and FY (C_{FY}) and MY (C_{MY}) sea ice concentrations. In particular, the NT algorithm makes use of the 19.35 ($T_{b,19}$), 22.24 ($T_{b,22}$), and 37.00 ($T_{b,37}$) GHz channels on SSM/I to compute ice concentrations and filter weather effects.

Assuming that space radiation is negligible, and that atmospheric contributions are generally negligible over the poles [6], the radiative transfer equation, which is valid for each frequency and polarization, can be modeled as

$$T_b = T_{b,OW}(1 - C) + T_{b,FY}C_{FY} + T_{b,MY}C_{MY}, \quad (2.4)$$

where $C = C_{FY} + C_{MY}$. To compute ice concentrations, the polarization ratio (R_P) and spectral gradient ratio (R_G) are defined as [25]:

$$R_P = \frac{T_{b,19V} - T_{b,19H}}{T_{b,19V} + T_{b,19H}}, \text{ and} \quad (2.5)$$

$$R_G = \frac{T_{b,37V} - T_{b,19V}}{T_{b,37V} + T_{b,19V}}. \quad (2.6)$$

Using the approximation that brightness temperature is equal to the product of surface emissivity and physical temperature, R_P and R_G are only a function of emissivity. Substituting Equation (2.4) into Equations (2.5) and (2.6) allows for the simultaneous solution for C_{FY} and C_{MY} . The solution is

$$C_{MY} = \frac{M_0 + M_1 R_P + M_2 R_G + M_3 R_P R_G}{D}, \text{ and} \quad (2.7)$$

$$C_{FY} = \frac{F_0 + F_1 R_P + F_2 R_G + F_3 R_P R_G}{D}, \quad (2.8)$$

where

$$D = D_0 + D_1 R_P + D_2 R_G + D_3 R_P R_G,$$

and where

$$\begin{aligned} M_0 &= A_4 B_0 - A_0 B_4, & F_0 &= A_0 B_2 - A_2 B_0, & D_0 &= A_4 B_2 - A_2 B_4, \\ M_1 &= A_5 B_0 - A_1 B_4, & F_1 &= A_1 B_2 - A_3 B_0, & D_1 &= A_5 B_2 - A_3 B_4, \\ M_2 &= A_4 B_1 - A_0 B_5, & F_2 &= A_0 B_3 - A_2 B_1, & D_2 &= A_4 B_3 - A_2 B_5, \\ M_3 &= A_5 B_1 - A_1 B_5, & F_3 &= A_1 B_3 - A_3 B_1, & D_3 &= A_5 B_3 - A_3 B_5, \end{aligned}$$

Table 2.1: Northern Hemisphere tie-points for the NT algorithm

Channel	T_b (Kelvins)		
	OW	FY	MY
$T_{b,19V}$	177.1	258.2	223.2
$T_{b,19H}$	100.8	242.8	203.9
$T_{b,37V}$	201.7	252.8	186.3

where

$$\begin{aligned}
A_0 &= -T_{b,OW,19V} + T_{b,OW,19H}, \\
A_1 &= T_{b,OW,19V} + T_{b,OW,19H}, \\
A_2 &= T_{b,MY,19V} - T_{b,MY,19H} + A_0, \\
A_3 &= -T_{b,MY,19V} - T_{b,MY,19H} + A_1, \\
A_4 &= T_{b,FY,19V} - T_{b,FY,19H} + A_0, \\
A_5 &= -T_{b,FY,19V} - T_{b,FY,19H} + A_1,
\end{aligned}$$

and where

$$\begin{aligned}
B_0 &= -T_{b,OW,37V} + T_{b,OW,19V}, \\
B_1 &= T_{b,OW,37V} + T_{b,OW,19V}, \\
B_2 &= T_{b,MY,37V} - T_{b,MY,19V} + B_0, \\
B_3 &= -T_{b,MY,37V} - T_{b,MY,19V} + B_1, \\
B_4 &= T_{b,FY,37V} - T_{b,FY,19V} + B_0, \\
B_5 &= -T_{b,FY,37V} - T_{b,FY,19V} + B_1.
\end{aligned}$$

The A and B values above provide a means of tuning the algorithm. The T_b values are the tie-points for OW, FY ice, and MY ice for the specified channels. Northern Hemisphere tie-points for the NT algorithm were obtained from [25] and are shown in Table 2.1.

Due to dispersion of T_b values by weather events, a weather filter was proposed by Cavalieri [24] that works as follows: If

$$\frac{T_{b,37V} - T_{b,19V}}{T_{b,37V} + T_{b,19V}} > 0.05,$$

and/or

$$\frac{T_{b,22V} - T_{b,19V}}{T_{b,22V} + T_{b,19V}} > 0.045,$$

then the sea ice concentration is set to zero.

The NT algorithm has been tuned for use with different platforms as they have become available. With the additional frequency channels available on AMSR-E, improvements to the NT algorithm were made resulting in the NT2 algorithm, which makes use of AMSR-E's 89 GHz channel to further filter weather effects. The NT algorithm and its variants are the operational standard for mapping Arctic sea ice concentration.

Chapter 3

Method of Sea Ice Investigation

Multiple approaches are used in this thesis to investigate the microwave characteristics of sea ice. Data is taken from different polarizations, frequencies, incidence angles, sensors, and algorithms. This chapter begins by describing a common method for the inter-comparison of this data. Briefly, data for each sensor are collocated using a common polar *stereographic projection*, with interpolation applied when applicable. Next, a joint analysis of passive and active microwave measurements is presented, including a discussion on the validity of using tie-points to represent FY ice, MY ice, and open water. Two methods are then described that are used to automatically determine data-clusters representative of FY ice, MY ice, and open water on a daily basis.

3.1 Data Preparation

To combine data from multiple sensors, their observations are converted to a common map projection known as a polar stereographic projection. A stereographic projection is a geometric mapping function that projects a sphere onto a plane. Although some distortion occurs, a stereographic projection is shape-preserving or orthomorphic. This means that circles of latitude and lines of longitude are preserved. For ease of data manipulation and storage in this thesis, projected results are rasterized (converted to pixels) with a nominal resolution of 4.45 pixels/km. A standard latitude of true scale at $N70^\circ$ is used. Intuitively, this projection compresses data at the pole and stretches it at the outside edge of the projection ($N60^\circ$). This is the standard projection used for BYU Scatterometer Climate Record Pathfinder (SCP) QuikSCAT egg SIR images (www.scp.byu.edu). AMSR-E image data in polar stereographic projection is also available from the SCP. These images are at a different pixel resolution and interpolated to the QuikSCAT pixels using bilinear interpolation. This

is advantageous over nearest neighbor interpolation, which tends to introduce discontinuities into the data. For example, discontinuities are observed when nearest neighbor interpolated data is compared with data at a higher resolution.

After collocation, a binary mask is applied to the data to standardize no-data regions between data sets and remove land. The brightness and contrast of land regions compared to ice and water tends to distort near-coast measurements. To reduce the effects of land, the land mask is dilated using binary dilation with a 5x5 pixel structuring element as described in [32]. Briefly, the land mask is dilated by projecting the structuring element centered over each pixel in the mask. The projected/dilated land mask and structuring element are shown in Figure 3.1. An example of binary dilation is shown in Figure 3.2.

3.2 Joint Analysis of Passive and Active Microwave Data

The motivation for a joint analysis of passive and active microwave data stems from several studies [33, 34, 35, 36, 37] that suggest that a more accurate characterization of sea ice may be accomplished using both active and passive microwave sensors rather than just using one type. The following subsections present analysis methods for analyzing passive and active data to estimate sea ice parameters.

3.2.1 Ratios of Brightness Temperature

The NT sea ice algorithm, which is reviewed in Chapter 2, defines a polarization ratio (R_P) and spectral gradient ratio (R_G), which serves to separate MY and FY ice. Equations (2.5) and (2.6) for R_P and R_G , respectively, are rewritten here to generalize their use:

$$R_P(f_1) = \frac{T_{b,f_1V} - T_{b,f_1H}}{T_{b,f_1V} + T_{b,f_1H}}, \text{ and} \quad (3.1)$$

$$R_G(f_1, f_2) = \frac{T_{b,f_2V} - T_{b,f_1V}}{T_{b,f_2V} + T_{b,f_1V}}, \quad (3.2)$$

where f_1 and f_2 represent the frequencies at which the brightness temperatures were measured. To apply R_G to AMSR-E, the 18.7 GHz and 36.5 GHz channels are selected for f_1 and

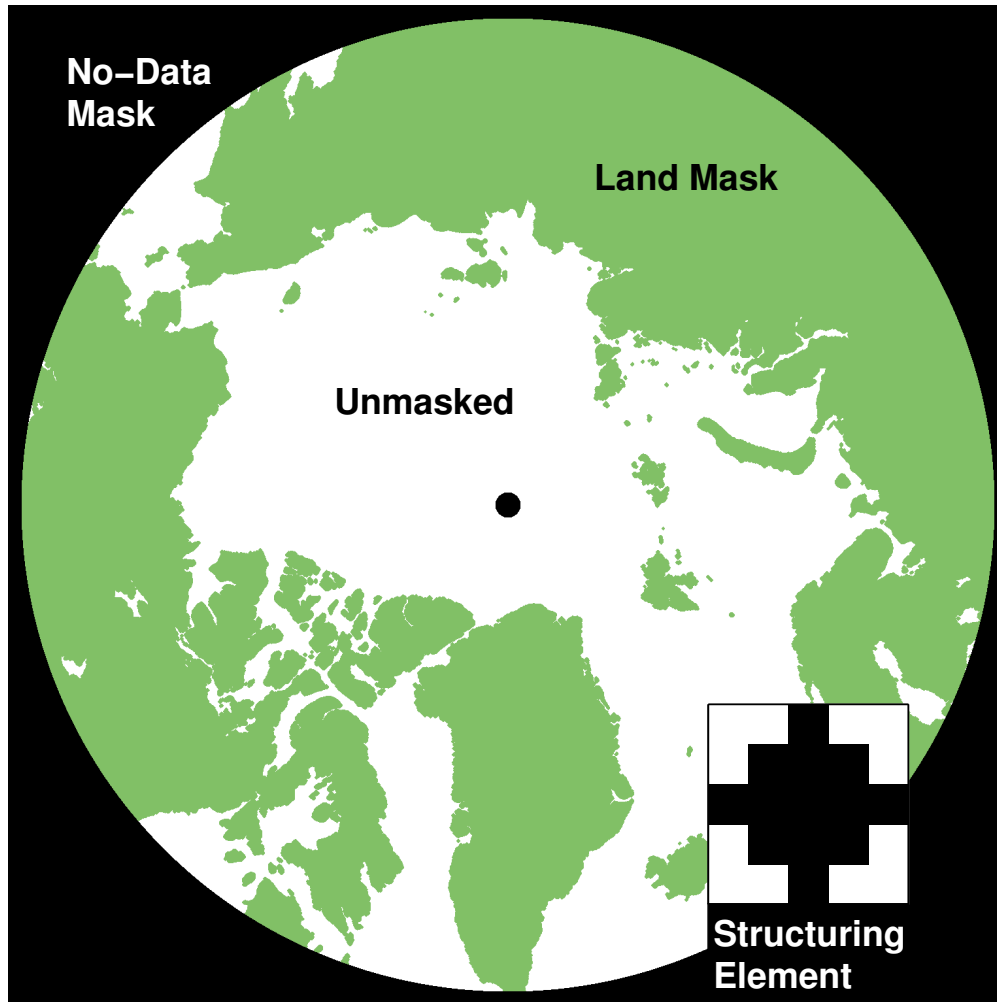


Figure 3.1: Arctic no-data and land mask in polar stereographic projection. The land mask is dilated using the shown structuring element to remove measurements with coastal effects.

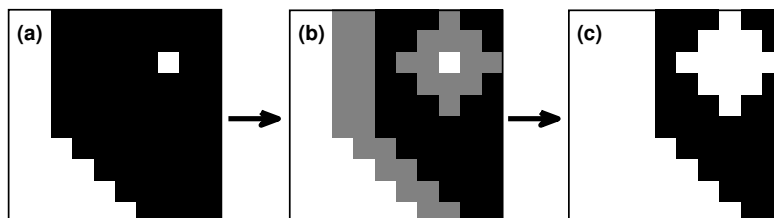


Figure 3.2: An example of binary dilation. (a) shows a sample binary mask (white), (b) shows pixels dilated by the structuring element (gray), and (c) shows the new mask.

f_2 respectively. These are similar to frequencies selected from the Special Sensor Microwave Imager (SSM/I) for which the NT algorithm has been calibrated.

We are interested in three different categories of Arctic surface cover: open water, FY ice, and MY ice. These surfaces exhibit a different appearance at different passive channel frequencies and polarizations. These differences can be exploited to map the extent of open water, FY ice, and MY ice. Consider the typical histograms of Arctic brightness temperatures shown in Figure 3.3. The histograms represent the V and H polarizations (V_{pol} and H_{pol}) of the 18.7 GHz channel of AMSR-E for DOY 15 in 2003. The leftmost mode for each polarization represents open water, followed by MY ice, and then FY ice. Interestingly, the brightness temperature difference between FY and MY ice is similar for each polarization, while the brightness temperature difference between open water and MY ice is twice as great for H_{pol} as for V_{pol} . The greater difference between open water and MY ice for H_{pol} is primarily due to the brightness temperature of the ocean at each polarization. In a simplified scenario that assumes a relatively smooth ocean surface, the brightness temperature (T_B) of open water can be modeled by (Equation (11.83) in [38]):

$$T_B(\theta, p) = [1 - \Gamma^{sp}(\theta, p)]T_0, \quad (3.3)$$

where θ is the angle of incidence from the surface zenith, p is the polarization, Γ is the specular surface reflectivity and T_0 is the physical temperature of the water. The specular surface reflectivity is given by (Equation (4.132) in [21]):

$$\Gamma^{sp}(\theta, H_{\text{pol}}) = \left| \frac{\mu_r \cos(\theta) - \sqrt{\mu_r \epsilon_r - \sin^2(\theta)}}{\mu_r \cos(\theta) + \sqrt{\mu_r \epsilon_r - \sin^2(\theta)}} \right|^2, \quad \text{and} \quad (3.4a)$$

$$\Gamma^{sp}(\theta, V_{\text{pol}}) = \left| \frac{\epsilon_r \cos(\theta) - \sqrt{\mu_r \epsilon_r - \sin^2(\theta)}}{\epsilon_r \cos(\theta) + \sqrt{\mu_r \epsilon_r - \sin^2(\theta)}} \right|^2, \quad (3.4b)$$

where μ_r is the relative magnetic permeability and ϵ_r is the relative complex dielectric constant of the surface. Using typical values of μ_r and ϵ_r for sea water, Figure 3.4 illustrates the greater emissivity calculated for V_{pol} compared to H_{pol} over a smooth ocean surface. The thick red line shows the incidence angle used by AMSR-E. The actual incidence angle at

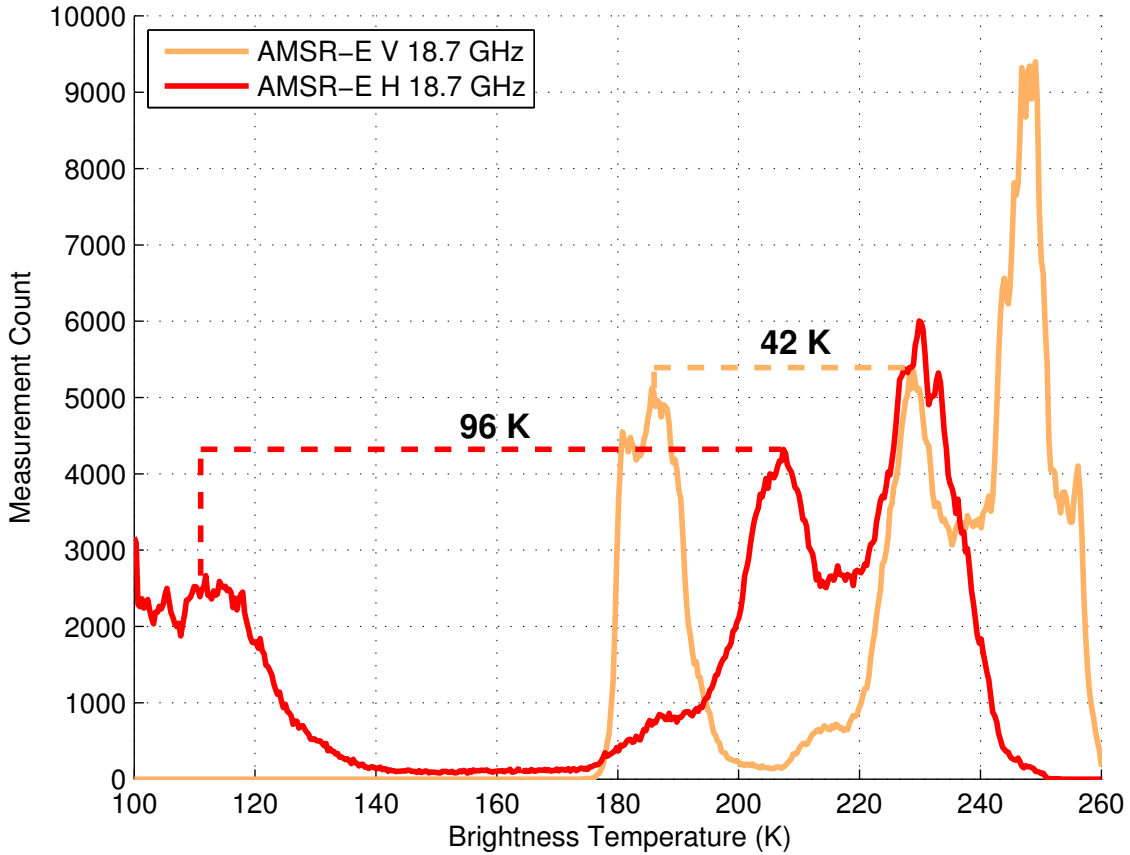


Figure 3.3: Typical histograms of AMSR-E V and H 18.7 GHz measurements during the winter. Each histogram has three modes representing open water, MY ice, and FY ice from left to right. The approximate distance between modes of open water and MY ice is shown for each histogram. Data is taken from DOY 15, 2003.

the ocean surface depends on the local surface, which varies with surface waves. However, in this model V_{pol} emissions are always greater than H_{pol} emissions. This observation is a motivating factor to use R_P .

The motivating factor for use of R_G can be seen in Figure 3.5. Here, open water has been removed, giving focus to the histograms of FY and MY ice. The figure illustrates a greater separation of FY and MY ice using the 36.5 GHz channel than seen for the 18.7 GHz channel. This is related to the source of microwave emissions from each ice type. Emissions come from the surface and volume of the ice. The salinity of FY ice makes it lossy, preventing significant emissions from the ice volume. However, emissions from MY ice, which is much

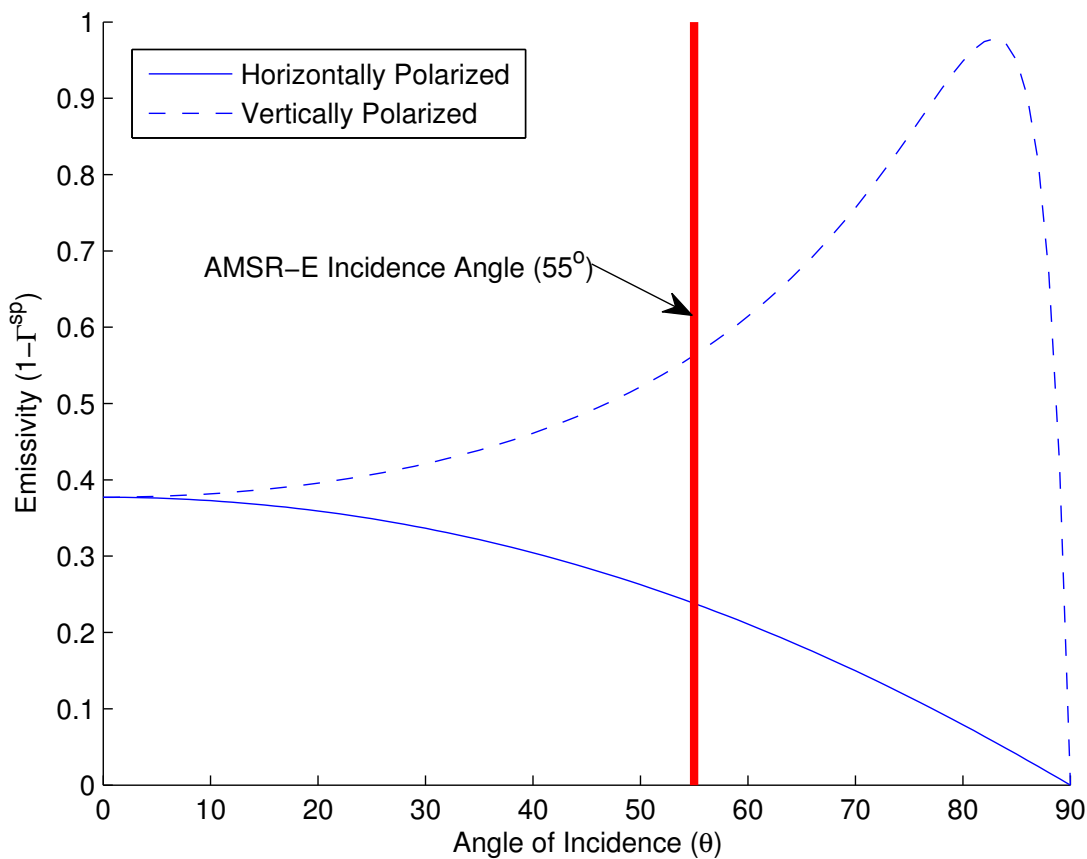


Figure 3.4: Calculated emissivity for horizontal (solid line) and vertical (dashed line) polarizations for $\mu_r = 1$ and $\epsilon_r = 54.4 - 36.8j$. These are typical values for sea water at 20° C with 36‰ salinity [27]. The solid red line shows the incidence angle used by AMSR-E.

less saline, have significant contributions from the ice surface and volume. As the observation frequency increases, emission depth decreases, reducing ice volume contributions. This effect can be seen in both FY and MY ice types, but is more pronounced in MY ice as observed in Figure 3.5. Generally, higher microwave frequencies are observed to result in greater separation of FY and MY ice, but have greater atmospheric sensitivity (to water vapor, rain, and snow for example).

A joint histogram of R_P and R_G illustrates the benefit of these ratios in Figure 3.6. R_P separates open water and ice, while R_G separates FY and MY ice. When calibrating the NT algorithm, which is done on a per sensor basis, tie-points are carefully selected to

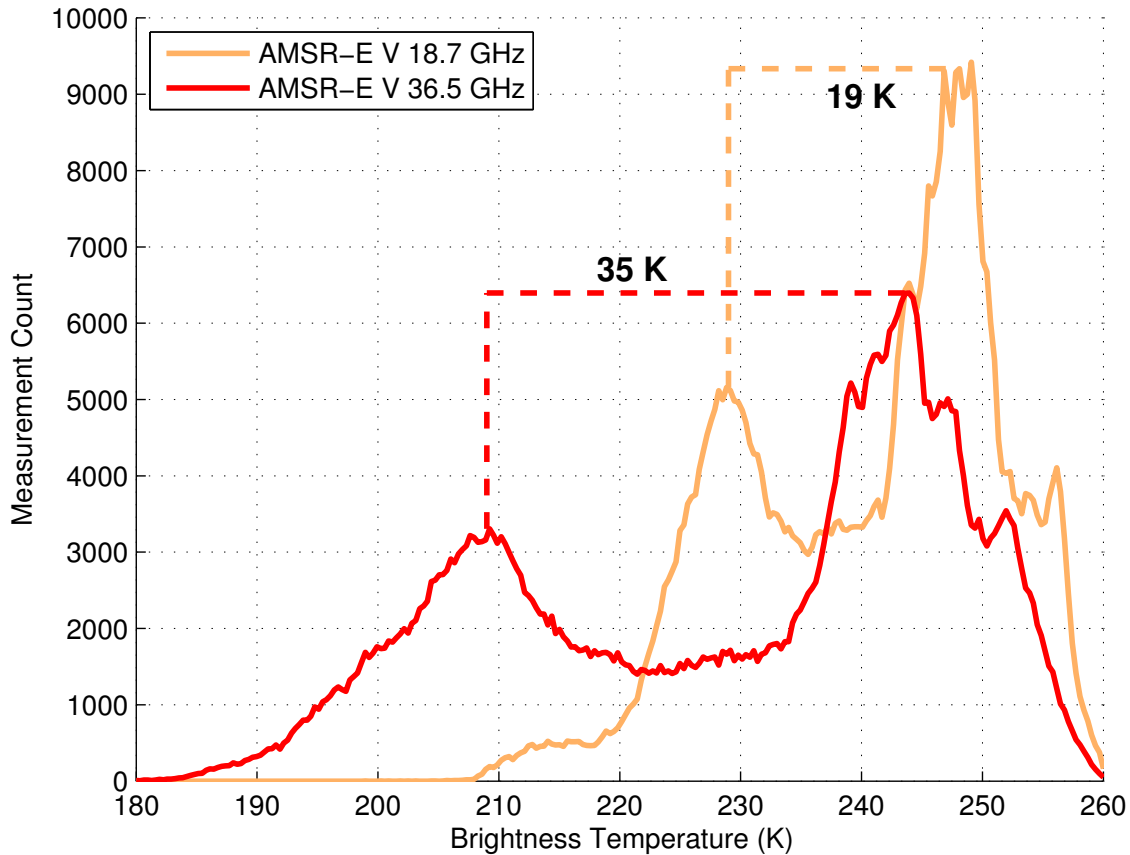


Figure 3.5: Typical histograms of AMSR-E V 18.7 GHz and V 36.5 GHz measurements over ice during the winter. Each histogram is bimodal where the left mode represents MY ice and the right mode represents FY ice. The approximate distance between modes is shown for each histogram. Data is taken from DOY 15, 2003.

represent the modes illustrated in Figure 3.6. Additional tuning is also employed in an effort to correlate calculated sea ice concentrations with ground truth [25].

3.2.2 Analysis with QuikSCAT

While the separation of modes representing sea ice type is demonstrated in Figure 3.6, sea ice may also be effectively separated using $R_G(18.7, 36.5)$ and QuikSCAT VV. Figure 3.7 shows a typical SIR image of QuikSCAT VV (a) and an image of $R_G(18.7, 36.5)$ (b), as well as a joint histogram (c) to illustrate the high (negative) correlation between them. In the joint histogram, the upper-left mode represents FY ice, and the lower-right MY ice.

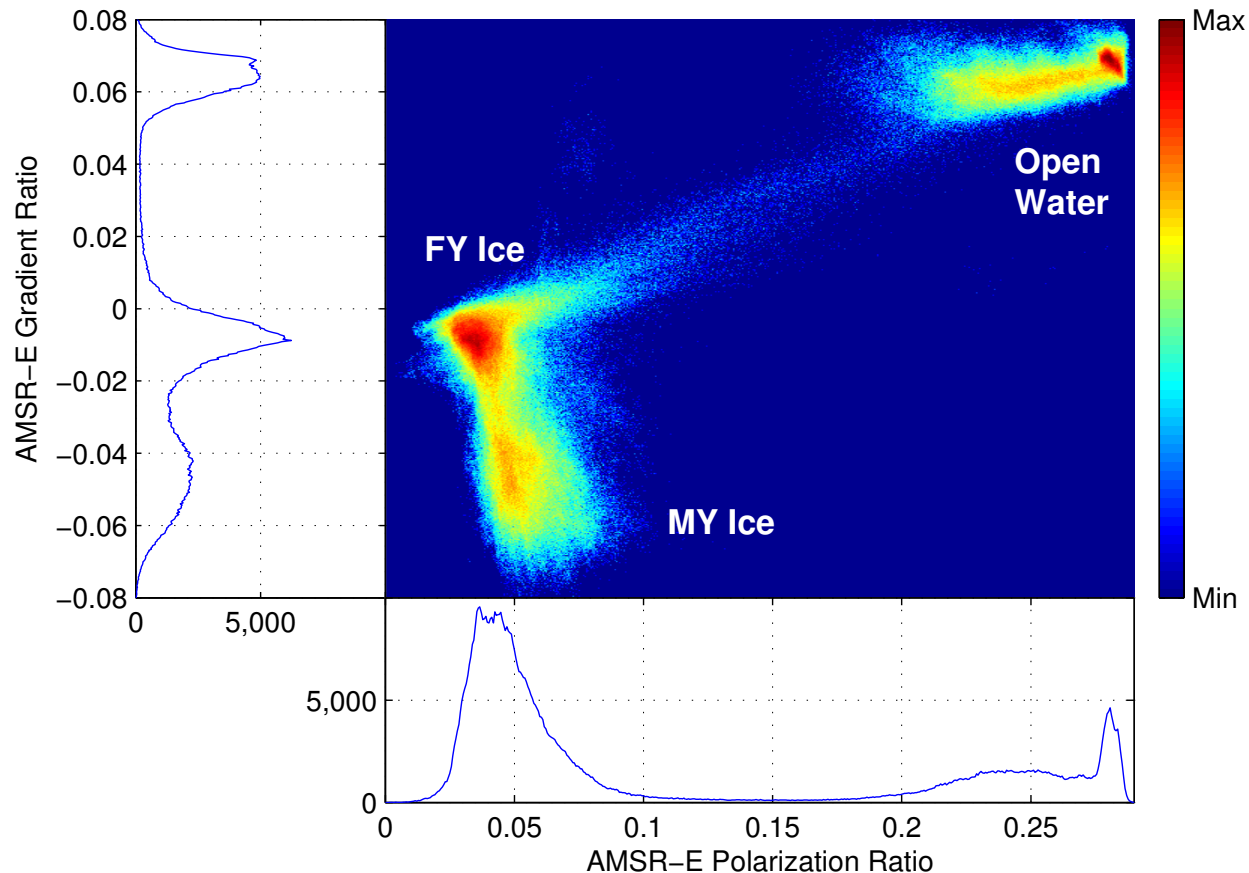


Figure 3.6: A joint histogram shows the relationship between R_P and R_G with marginal histograms shown to the left and bottom. The joint histogram has been log-height scaled to show more detail. Data is taken from DOY 15, 2003.

Interestingly, the joint histogram illustrates that FY ice has less variance in the AMSR-E R_G dimension than in the QuikSCAT VV dimension. The opposite is true for MY ice. These observations hold during the winter.

3.3 Variability in Sea Ice Signatures

The validity of using fixed sea ice signatures (tie-points) is independent of whether the NT algorithm or an active/passive microwave approach is employed for sea ice classification. Tie-points have been traditionally determined as the modes of the distributions at a fixed time or averaged over a particular time period. However, the modes associated with R_P and R_G vary over the season and are not constant. Figure 3.8 shows joint histograms of R_P and R_G for two days selected from the 04-05 winter where the modes have been highlighted by

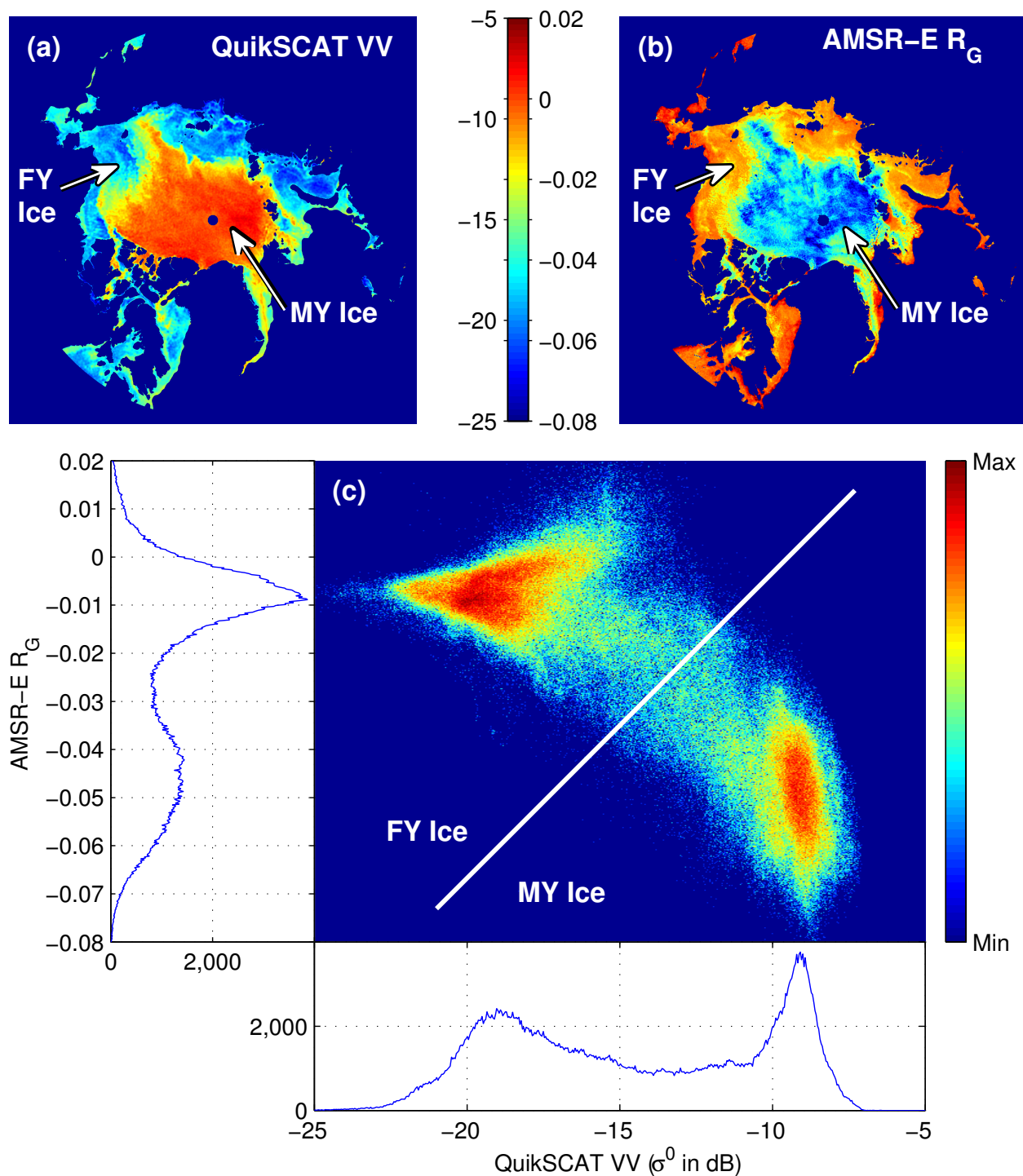


Figure 3.7: SIR images of both (a) QuikSCAT VV and (b) AMSR-E gradient ratio (R_G) show clear separations in FY and MY ice. (c) A joint histogram shows the relationship between these two data sets for measurements over ice with marginal histograms shown to the left and below. The line shows an approximate separation of FY and MY ice. The joint histogram has been log-height scaled to show more detail. Ocean has been removed using a mask. Data is taken from DOY 15, 2003.

solid squares in (a) and solid circles in (b). These annotations are replicated as dashed shapes in each image for comparison. In (b), the modes for FY and MY ice are closer together than in (a). This example suggests that fixed tie-points may not be the best approach.

In an effort to determine whether fixed or daily-varying sea ice signatures are more appropriate, two different methods are derived for selecting seasonally-varying tie-points. Initially, probability distributions for each ice type and open water are sought. Single values can then be derived from the resulting distributions. The first method is to use histograms with spatial processing. The second is to use an automated clustering algorithm with spatial processing.

3.3.1 Histogram Estimation

The histogram estimation method is performed in three steps: (1) form a rough classification of FY and MY ice to select spatially homogeneous areas, (2) refine the classification to commonly recurring measurements, and (3) spatially dilate and erode the refined classification.

As noted earlier, R_P is useful for distinguishing sea ice and open water. Similarly, QuikSCAT VV is useful for distinguishing FY and MY ice. Histograms of $R_P(18.7)$ and QuikSCAT VV are shown in Figure 3.9. To form rough classifications of sea ice and open water, the minimum bin between maximums of the $R_P(18.7)$ histogram is used as a threshold. A threshold is similarly selected to classify FY and MY ice. Rough classifications are shown in Fig. 3.10.

The next step is to reduce each rough classification (FY ice, MY ice, and open water) to densely clustered measurements. $R_G(36.5, 18.7)$ is well-suited to this purpose during the winter because it is sensitive to transitions among FY ice, MY ice, and open water, but it is insensitive to wind over the ocean [23] or to the physical temperature variation over the ice. When $R_G(36.5, 18.7)$ is restricted to one of the rough classifications, it is singly distributed. The mode is assumed to be representative of the classified surface type, rather than a mixture of ice and water. This histogram is used to refine the rough classification by selecting measurements that fall immediately around the mode. In particular, the classification is arbitrarily restricted by selecting measurements from the histogram where the height of the

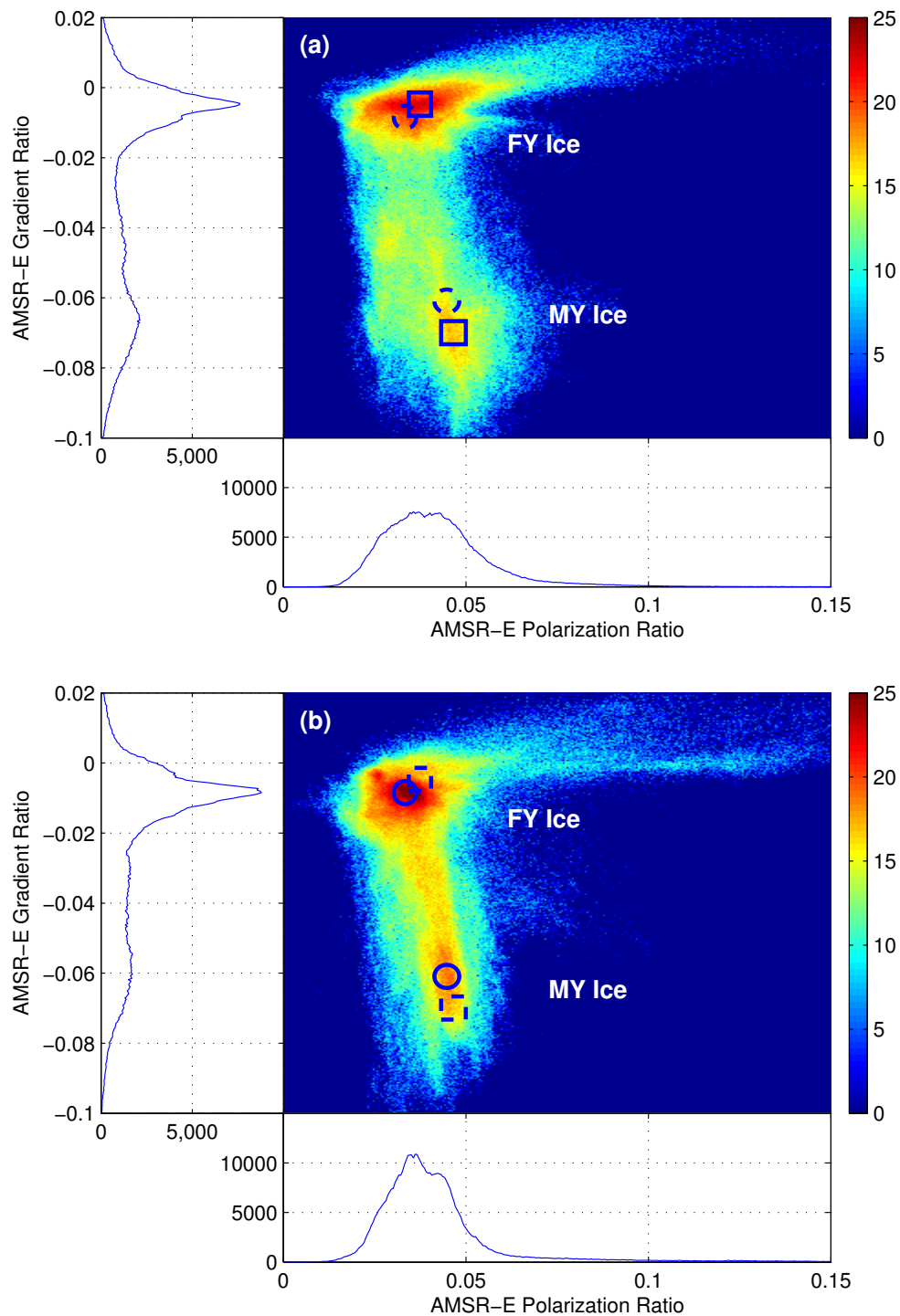


Figure 3.8: Joint histograms of R_P and R_G for (a) DOY 336, 2004 and (b) DOY 32, 2005 with marginal histograms shown to the left and bottom. Approximate modes are annotated by solid squares in (a) and solid circles in (b). These annotations are replicated as dashed shapes in each image for comparison. The joint histograms have been log-height scaled to show more detail.

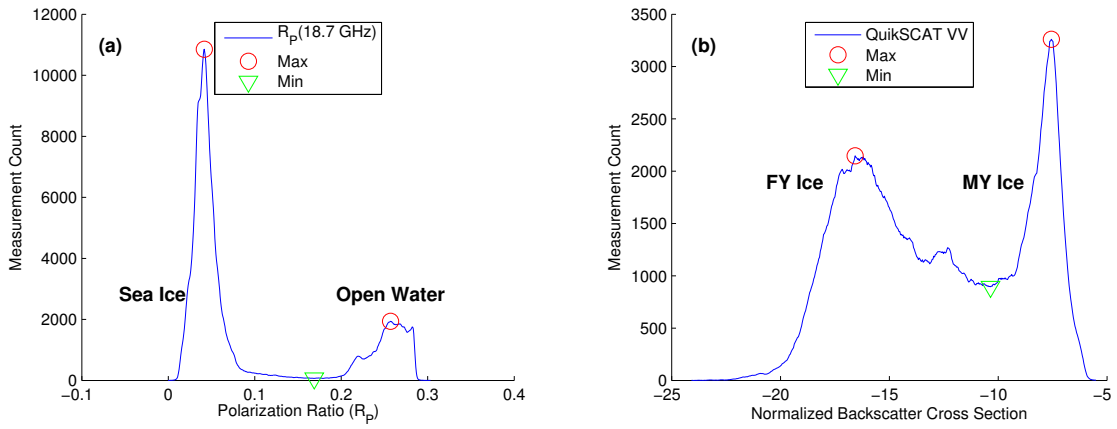


Figure 3.9: Histograms of (a) AMSR-E $R_P(18.7)$ and (b) QuikSCAT VV measurements. Each histogram is bimodally distributed with maximums and minimum (between maximums) marked. Data is taken from DOY 32, 2003.

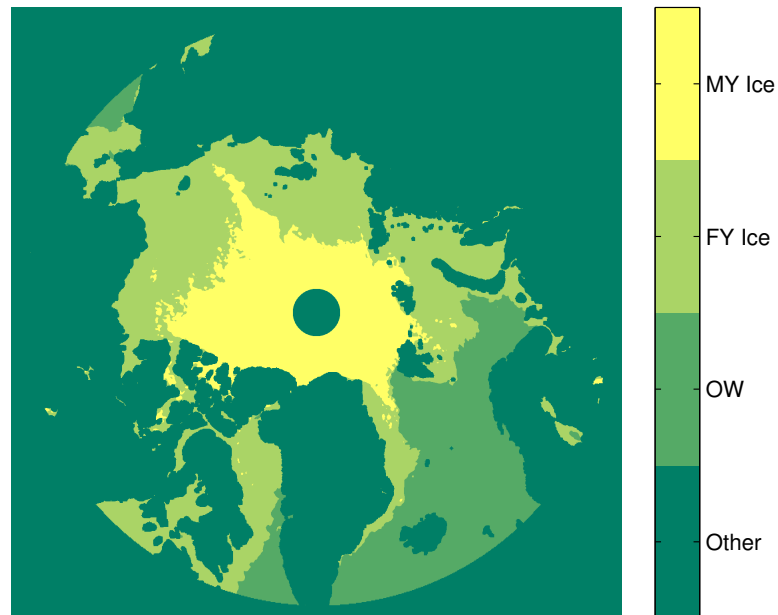


Figure 3.10: Rough classifications for OW, FY ice, and MY ice over the Arctic for DOY 32, 2003.

histogram is more than half of the height of the mode. Figure 3.11 shows selected subsets for FY ice, MY ice, and open water classifications. Measurements that fall between the left and right dashed lines form the refined classification.

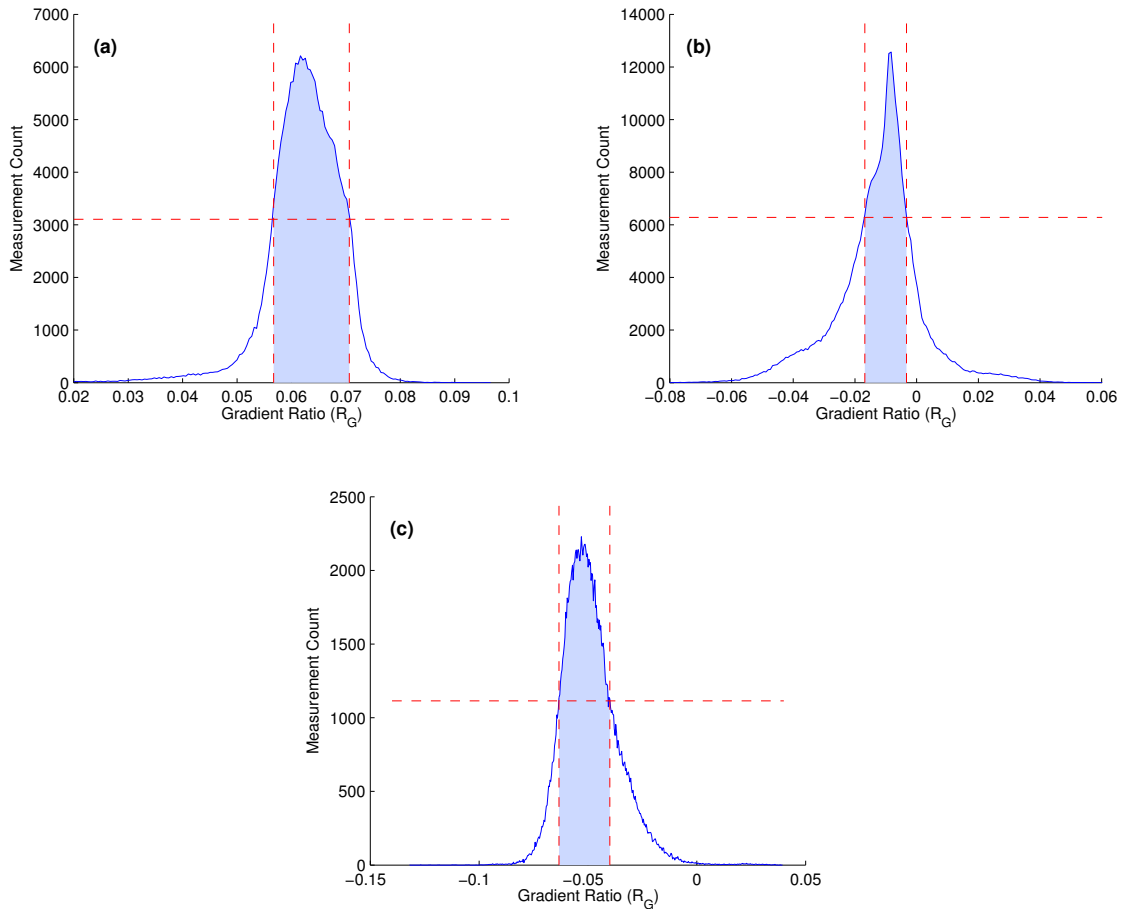


Figure 3.11: Restricted distribution of $R_G(36.5, 18.7)$ under the rough (a) open water, (b) FY ice, and (c) MY ice classifications. The dashed lines represent the restriction which is based on half the height of the mode. Data is taken from DOY 32, 2003.

The final step is to improve spatial consistency by spatially dilating and eroding each refined classification. Eroding has the effect of removing sparse regions, and dilating has the effect of spatially connecting concentrated regions. The final classifications are shown in Figure 3.12. Notice that, as a result of processing, transitional areas have been removed from the set of final classifications in contrast to the rough classifications in Figure 3.10.

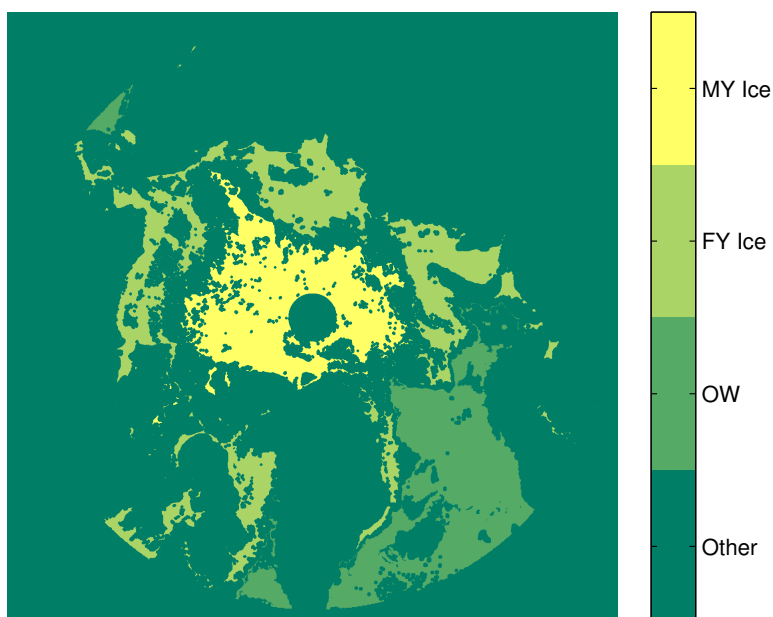


Figure 3.12: Final classifications for OW, FY ice, and MY ice for DOY 32, 2003.

This ensures that the final area consists purely of a single surface class. Note that this classification is not intended to apply to all ice-covered areas. Instead, it selects areas of pure ice classes.

In an attempt to apply this approach over an entire winter, it becomes apparent that a clear maximum does not always exist for one-dimensional histograms of measurements from each surface class. In an effort to develop a more robust classification method, a multi-dimensional cluster approach is used, which can take advantage of the large number of available data channels.

3.3.2 Multi-dimensional Clustering Algorithm

The OPTICS (Ordering Points To Identify the Clustering Structure) algorithm [39] is used in an attempt to determine distributions of sea ice type and open water. The OPTICS algorithm uses a density-based clustering strategy to partition data into meaningful groups. An important motivation for use of the OPTICS algorithm comes from its ability to detect

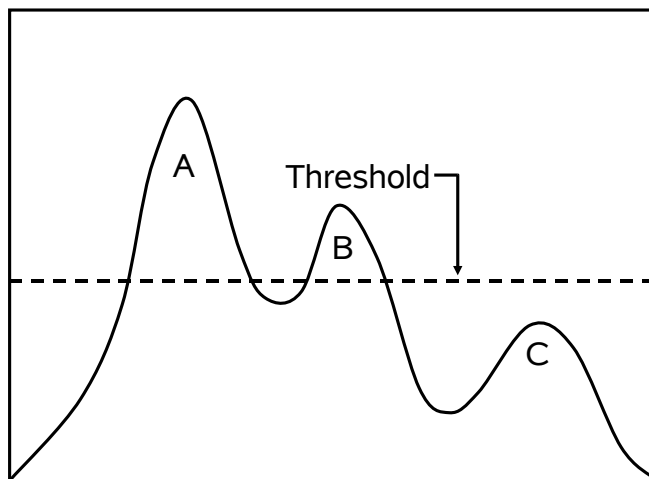


Figure 3.13: Histogram of points on a line demonstrating the difficulty of detecting clusters with a threshold.

clusters with varying densities without prior knowledge. Figure 3.13 illustrates a histogram of points along a line. Three clusters are present. Using the illustrated threshold, clusters A and B are detected, but C is missed. By adjusting the threshold, C can be detected, but A and B are assigned to the same cluster. This can be overcome by scanning over multiple thresholds, which is effectively what the OPTICS algorithm does.

Another motivation for the use of the OPTICS algorithm comes from its ability to map multi-dimensional data to two-dimensions using a distance metric and the order in which it processes points. Such a plot is known as a *reachability plot*.

The following list contains several definitions which are useful to the OPTICS algorithm. Many of these are borrowed from the DBSCAN algorithm, from which the OPTICS algorithm is adapted.

1. An object P is in the ϵ -**neighborhood** of Q if the distance from P to Q is less than ϵ (Figure 3.14-A).
2. A **core object** has at least *MinPts* in its ϵ -neighborhood (Figure 3.14-B where *MinPts* = 4).

3. An object P is **directly density-reachable** from object Q if Q is a core object and P is in the ϵ -neighborhood of Q (Figure 3.14-C).
4. An object P is **density-reachable** from an object Q if there is a chain of objects P_1, \dots, P_n , where $P_1 = Q$ and $P_n = P$ such that P_{i+1} is directly density reachable from P_i (Figure 3.14-D).
5. An object P is **density-connected** to an object Q if there is an object O such that both P and Q are density-reachable from O (Figure 3.15-A).
6. A **cluster** is a set of density-connected objects which is maximal with respect to density-reachability. Noise is the set of objects not contained in any cluster (Figure 3.15-B).
7. The **generating-distance** ϵ is the largest distance considered for clusters. Clusters can be extracted for all ϵ_i such that $0 \leq \epsilon_i \leq \epsilon$ (Figure 3.16).
8. The **core-distance** is the smallest distance ϵ' between a core object Q and an object P in its ϵ -neighborhood such that a radius at ϵ' around Q contains exactly *MinPnts* (Figure 3.16).
9. The **reachability-distance** of P is the smallest distance such that P is density reachable from a core object Q. Additionally the reachability distance of P must be at least as large as the core-distance of Q (Figure 3.16).

Starting at a user defined point, OPTICS uses a priority queue to process neighbors in order of reachability distance where priority is given to the smallest distance. Every point is processed only once during which its core distance and reachability distance are written to an ordered list of points. Figure 3.17 provides a flowchart of the complete algorithm.

A *reachability plot*, which is a plot of reachability-distance versus point ordering, is used to interpret results. Figure 3.18 shows a reachability plot for three random clusters. In a reachability plot, valleys in the point ordering represent points that belong to a cluster. Peaks are caused by points that are distant from clusters. It is interesting to note that Figure 3.18 has a hierarchical structure where two of the valleys are contained in a larger

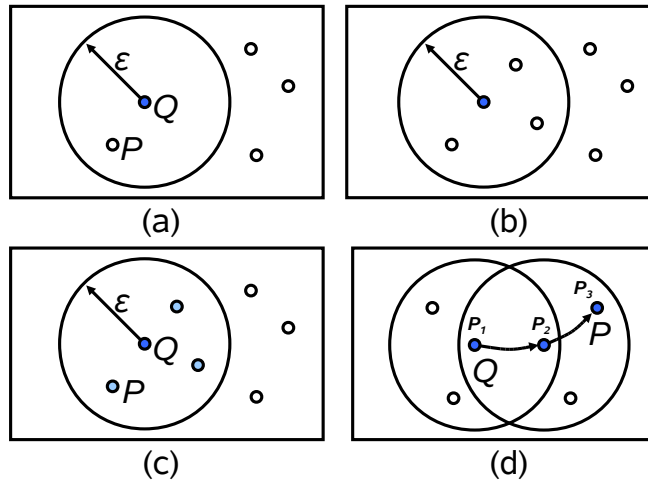


Figure 3.14: OPTICS Definitions: (a) P is in the ϵ -Neighborhood of Q . (b) The center point is a core object ($MinPnts = 4$). (c) Points inside the circle (such as P) are directly density-reachable from Q . (d) P is density reachable from Q . See text.

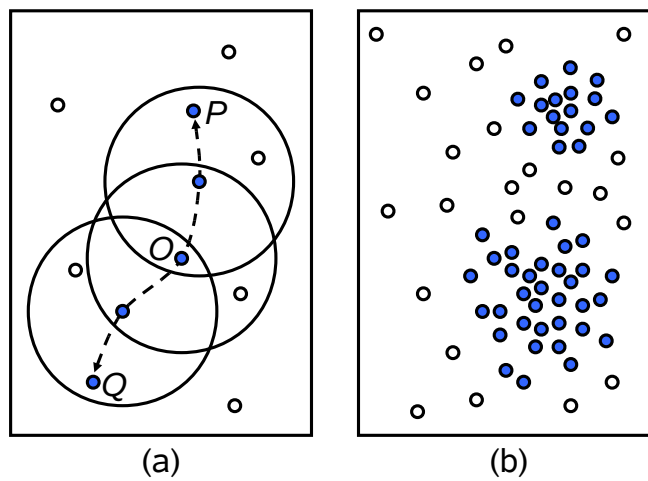


Figure 3.15: OPTICS Definitions: (a) P is density connected to Q (b) Solid points belong to clusters. Other points are noise. See text.

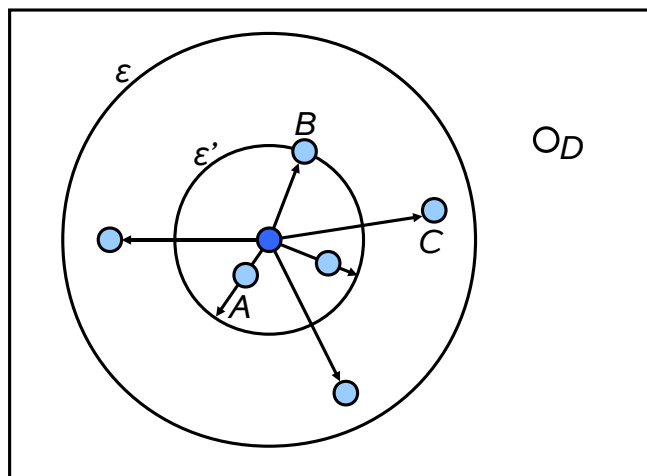


Figure 3.16: OPTICS Definitions: Arrows represent reachability distance. Point A is inside the core-distance radius. Point B sets the core-distance for $MinPnts = 4$. Point C is outside the core, but inside the generating distance. Point D is outside the generating distance. It has UNDEFINED reachability-distance. See text.

valley. This is correctly interpreted as two clusters being closer to each other than to the third cluster.

As a final step in the algorithm, clusters are automatically detected from the reachability plot. This is done hierarchically using a set of definitions that are not repeated here. The detection relies on a steepness parameter which is a percentage change in reachability distance from one point to the next.

The OPTICS algorithm appears to function best when each dimension is scaled similarly. To accomplish this, each dimension is normalized before the algorithm is applied using

$$\hat{M}_i = \frac{M_i - \min\{M\}}{\max\{M\} - \min\{M\}}, \quad (3.5)$$

where M is the set of measurements from a single dimension, the subscript i represents an index into the set M , and $\min\{\}$ and $\max\{\}$ return the minimum and maximum values of a set respectively.

Figure 3.19 shows a reachability distance plot generated by the OPTICS algorithm for a two-dimensional data set consisting of AMSR-E R_G and QuikSCAT VV (see also Figure

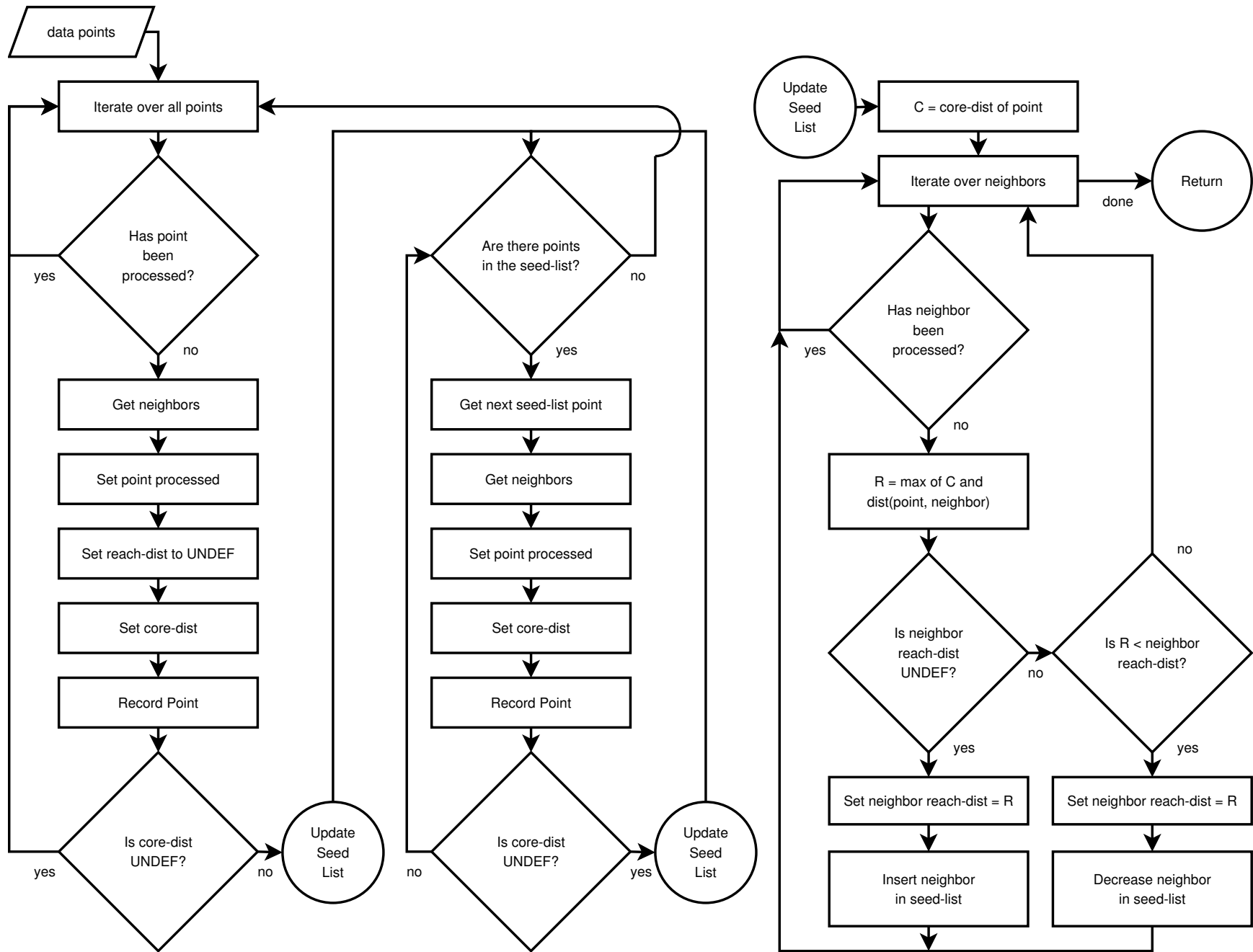


Figure 3.17: The OPTICS Algorithm

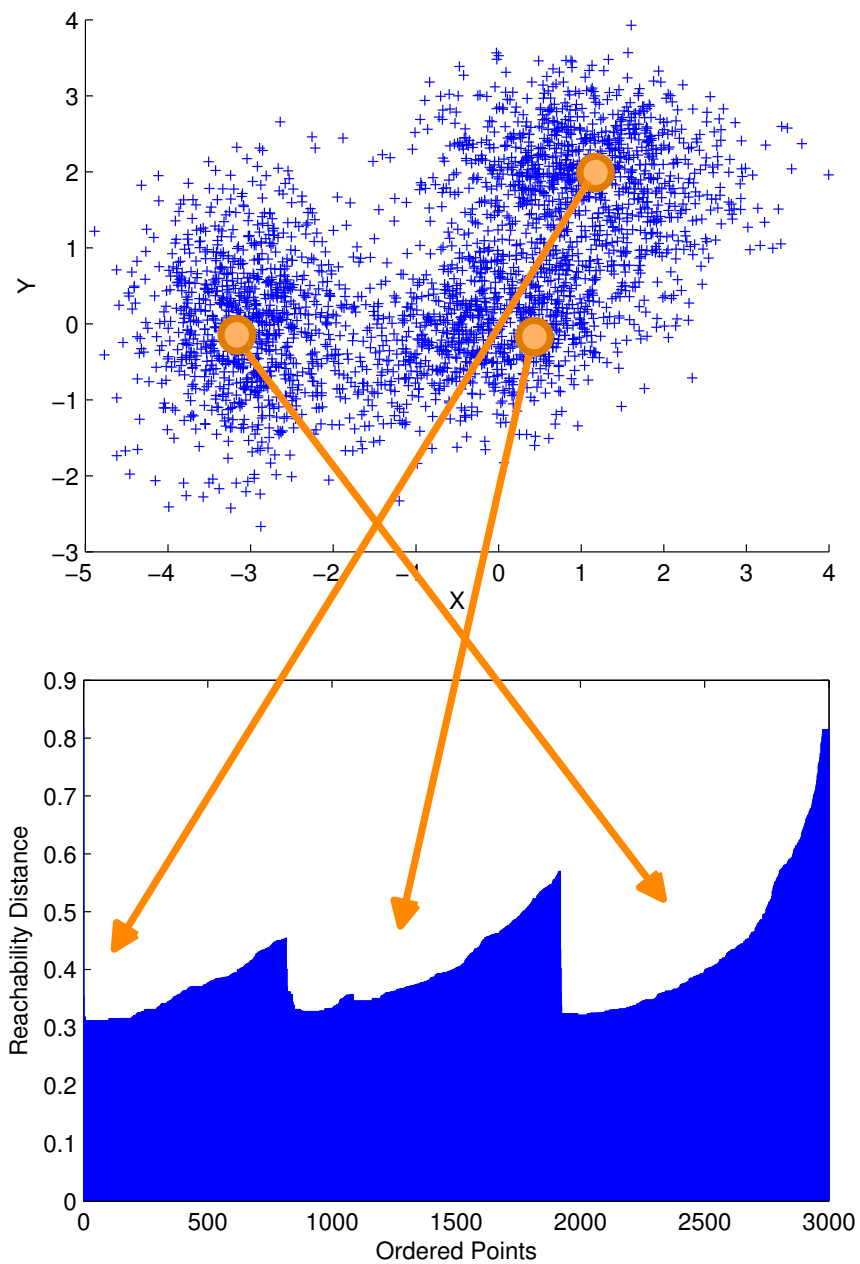


Figure 3.18: Reachability plot example for three random clusters. The relationship between clusters and valleys is indicated by arrows. MinPnts is set to 100.

3.7(c)). The clustering structure is hierarchical. Open water and sea ice are identified as higher level clusters, and FY and MY ice are contained within the sea ice cluster. Figure 3.20 shows a mapping of these clusters back onto AMSR-E R_G to show that the clusters represent each surface class.

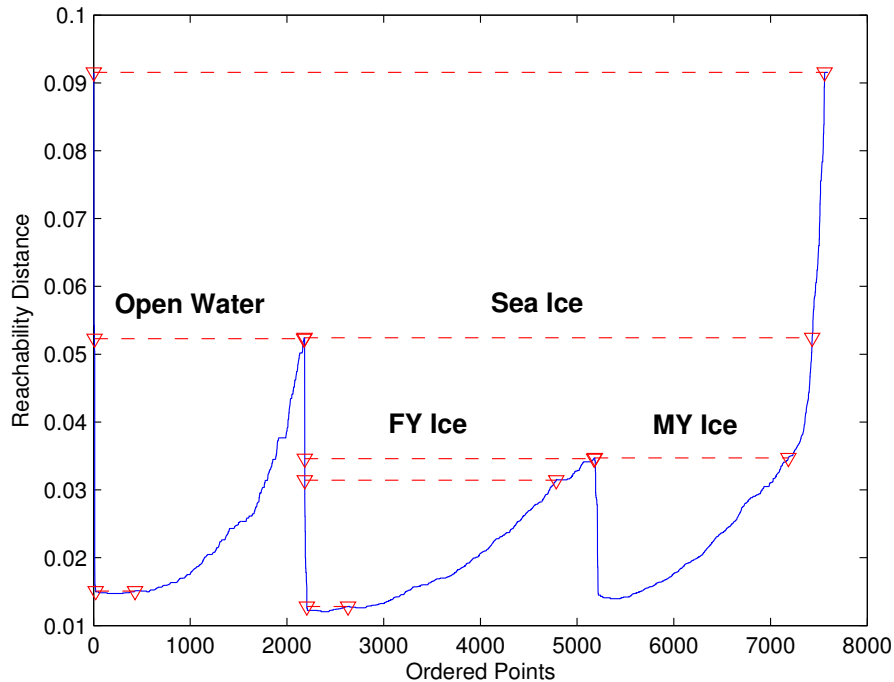


Figure 3.19: Reachability distance plot generated by the OPTICS algorithm for a two-dimensional set consisting of AMSR-E R_G and QuikSCAT VV. The red dashed lines terminated by triangles indicate sets of points within a cluster. This plot only represents 1 out of every 100 points to reduce excessive detection of clusters and increase processing speed. Data is taken from DOY 15, 2003.

The OPTICS algorithm is a promising method for determining distributions associated with sea ice type and open water. However, in favor of a simpler method, the following chapters describe a two step process to classify sea ice, where classification is based on a model derived from historical averages. This process produces similar results to the OPTICS algorithm, but has better year-to-year consistency since the same thresholds are used for each year.

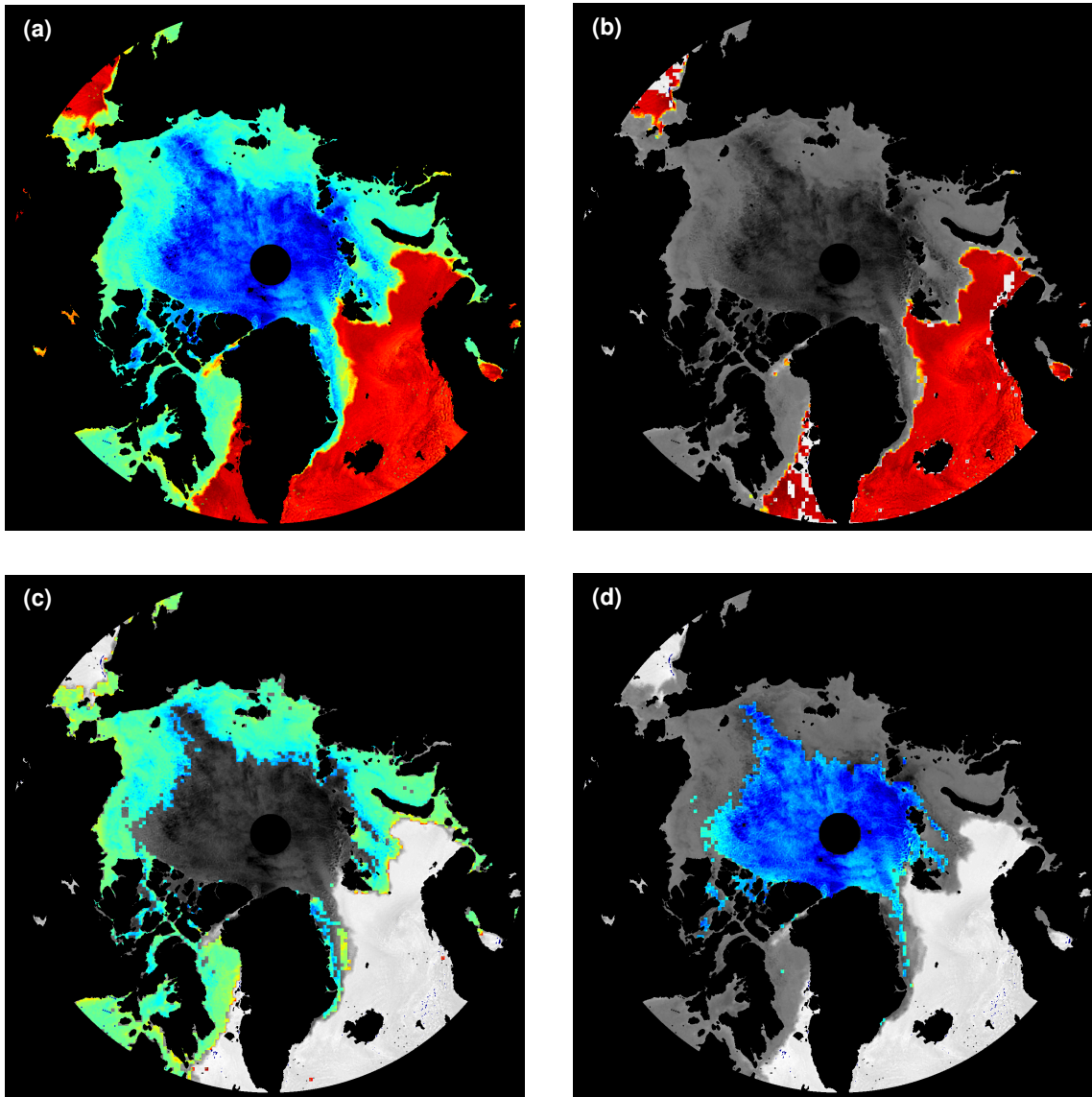


Figure 3.20: Clusters determined using the OPTICS algorithm are mapped over AMSR-E R_G . Clusters are shown in color. (a) is an all-inclusive cluster, (b) represents open water, (c) represents FY ice, and (d) represents MY ice. Data is taken from DOY 15, 2003.

Chapter 4

Intra- and Interannual Sea Ice Trends

The previous chapter presented an investigation of backscatter signatures over open water, FY ice, and MY ice. In this chapter, time series of histograms of backscatter over sea ice are analyzed. The intent is to create a sea ice classification model based on the day of the year. For this analysis, a method of separating sea ice and open water is first employed, then backscatter ice statistics are computed. Observed seasonal trends are then presented with speculation as to their physical cause. This chapter concludes with a summary of findings.

4.1 Isolating High Sea Ice Concentrations

For the purposes of developing a model, we exclude backscatter measurements over open water and low sea ice concentrations. This initial step effectively excludes the marginal ice zone (MIZ) where open ocean processes (particularly waves) significantly influence the properties of sea ice. Although QuikSCAT measurements are sensitive to the ocean-ice interface, high winds often cause measurements over the ocean to appear like ice. High winds can make it difficult to isolate high ice concentrations using QuikSCAT. However, brightness temperatures obtained from the 6 GHz V (or H) channel of AMSR-E ($A_{6,V}$) show a high contrast between ocean and ice. AMSR-E SIR images are high resolution and span largely the same time frame as QuikSCAT. They are also readily available and are collocated with QuikSCAT measurements. The contrast between open water and FY ice, with respect to emissivity (and brightness temperature), increases as frequency decreases [40]. This is possibly due to increased ice volume emissions from increased emission depth at lower frequencies, which is discussed in Chapter 3. Applying a fixed threshold to $A_{6,V}$ is a simple and adequate method to remove measurements over the ocean and the MIZ. Using

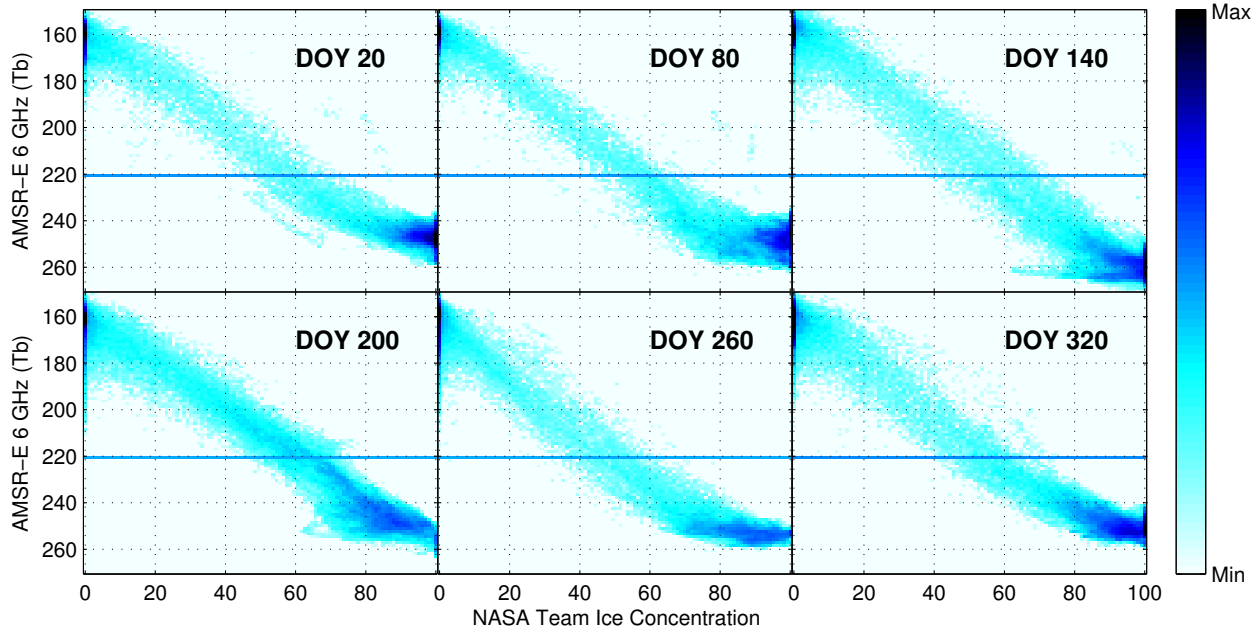


Figure 4.1: Typical joint histograms of AMSR-E 6 GHz V brightness temperatures and ice concentrations from the NASA Team algorithm for selected days of the year (DOY) in 2004. Histogram bins have been log height scaled. The horizontal line represents a threshold at 220 K.

one of the previously mentioned sea ice concentration algorithms may also be appropriate for this purpose.

To illustrate the sensitivity of $A_{6,V}$ to sea ice concentration, a comparison is made with ice concentration maps produced by the NASA Team (NT) sea ice algorithm [25, 24]. The NT ice concentrations (which are provided in polar stereographic projection) were resampled using bilinear interpolation for comparison. Figure 4.1 shows typical joint histograms of NT ice concentrations and $A_{6,V}$ measurements from 2004. In each case, a high correlation between $A_{6,V}$ and the NT ice concentration is evident. Areas with $A_{6,V}$ brightness temperatures above 220 K correspond to winter sea ice concentrations of 40 percent or more. For illustration, the 220 K threshold is shown in Figures 4.1 and 4.3. We note here that the observed distributions of QuikSCAT measurements corresponding to pixels above the threshold are not sensitive to the exact threshold on $A_{6,V}$.

An advantage of using only $A_{6,V}$ is its lack of sensitivity to ice type, which prevents a bias toward the selection of FY or MY ice. A typical SIR image of $A_{6,V}$ is shown in Figure 4.2, where ocean and ice measure approximately 160 K and 250 K respectively. There is

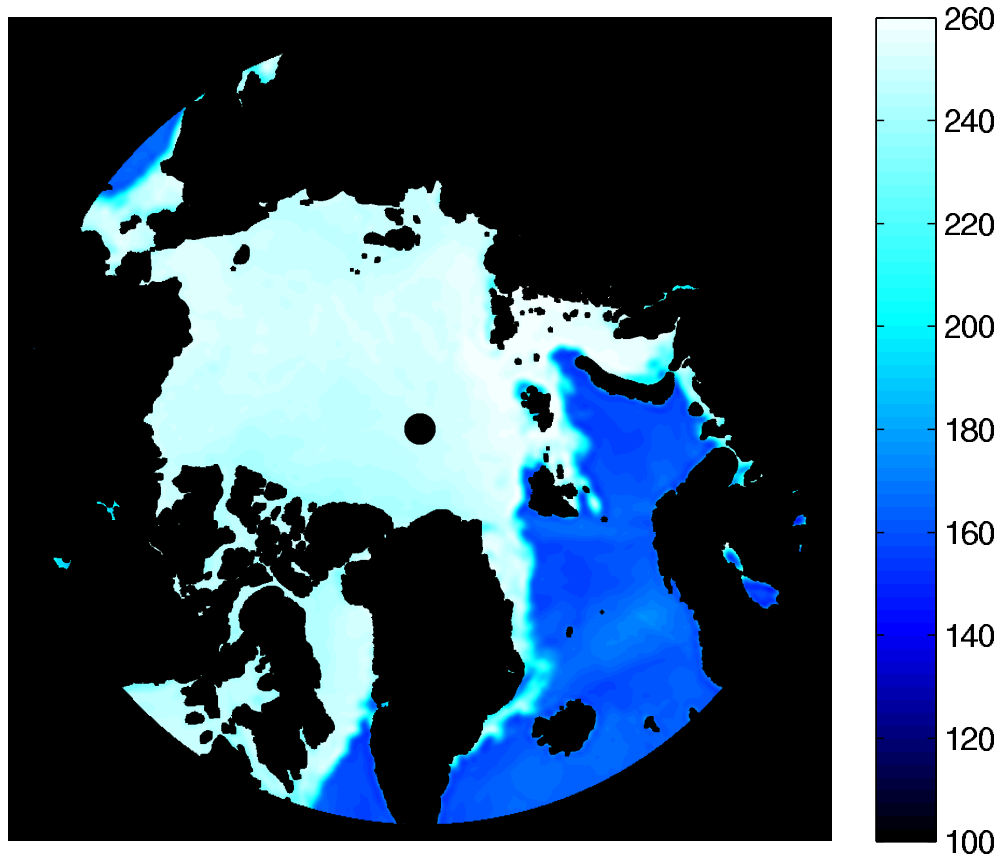


Figure 4.2: AMSR-E 6 GHz V brightness temperatures (K) over the Arctic on DOY 32, 2005 (land has been excluded). The ocean and ice measure approximately 160 K and 250 K respectively.

no clear distinction between FY and MY ice at this frequency. For reference, MY ice is typically located north of Greenland's coast and in the vicinity of the north pole. Figure 4.3 contains a time series of histograms during 2004 of $A_{6,V}$. The mode along the top of the figure represents ocean, while the varying mode at the bottom represents ice. Except during the summer (days 150 to 250), measurements over FY and MY ice are indistinguishable in $A_{6,V}$.

A typical derived sea ice mask created using this threshold approach is shown applied to a QuikSCAT SIR image in Figure 4.4 for DOY 20, 2004. Ocean has been removed by the mask. Land has been removed using a standard Arctic land mask.

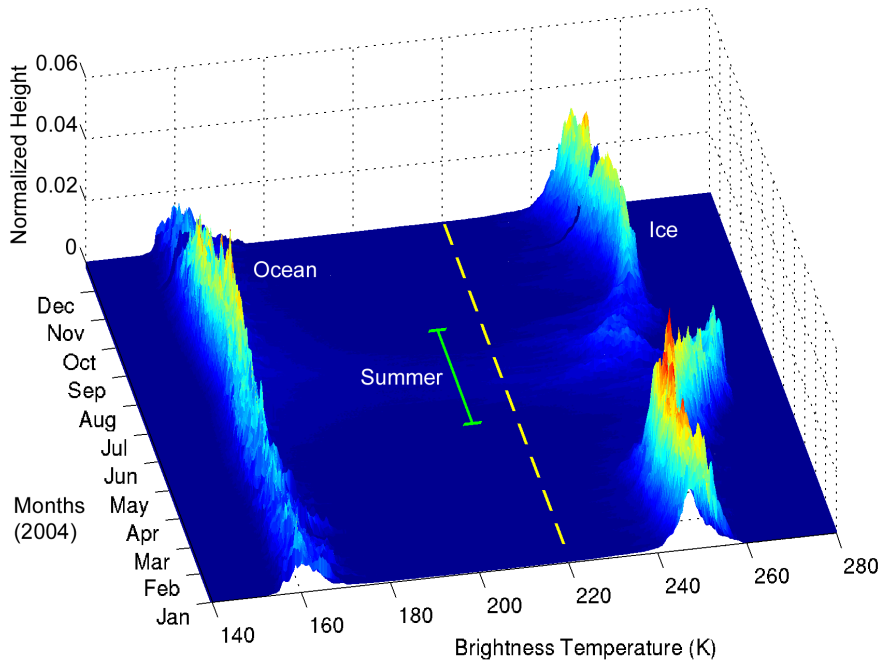


Figure 4.3: A daily time series of histograms of AMSR-E 6 GHz V brightness temperatures over the Arctic during 2004. Histograms are normalized and exclude measurements over land. The dashed line represents a threshold separating modes representative of ocean and ice. The summer melt period is indicated by a solid line.

4.2 Temporal Trends Observed in QuikSCAT Measurements

During the winter, active microwave measurements from QuikSCAT are characteristically bright over MY ice while lower returns are seen over FY ice. Some of the distinction between ice types is due to differences in ice salinity, porosity, surface roughness, and ridges on the order of meters to kilometers in length. Analyses of satellite scatterometer data show a large dynamic range of Ku-band backscatter, which has a strong sensitivity to FY and MY ice [41].

Understanding the temporal nature of sea ice backscatter allows and/or improves the classification of ice as FY or MY. To visualize temporal sea ice characteristics, we use a time series of histograms of QuikSCAT measurements. Figure 4.5 shows a series of histograms for the winter of 06-07 where sea ice has been selected using the method described in Section 4.1 and the histograms have been normalized. The distribution from each day during the winter has approximately one large mode around -20 dB representing FY ice, and one large mode

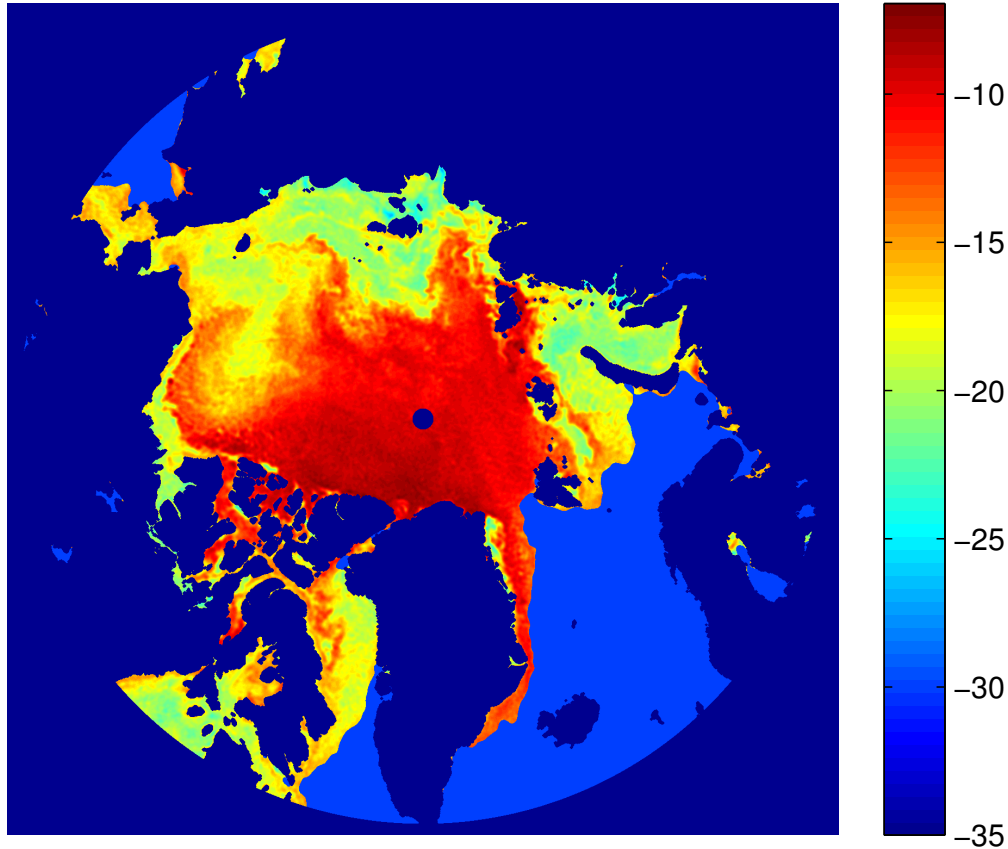


Figure 4.4: A typical SIR image of QuikSCAT VV (σ^0 in dB). The ocean has been masked by applying a threshold to collocated AMSR-E brightness temperatures. (DOY 20, 2004).

around -10 dB with some smaller modes above -10 dB representing MY ice. At Ku-band, σ^0 for FY ice is approximately -25 to -18 dB and MY ice is approximately -10 to -12 dB [20].

4.2.1 Trends in First-Year Ice

Similar to Figure 4.5, the winter of 04-05 is shown in Figure 4.6(a), where the perspective is now rotated and viewed from top down. Figure 4.6(a) provides evidence that the microwave signature of FY ice is seasonally dependent. The pattern shown in Figure 4.6(b) approximately describes the behavior of FY ice backscatter for every year between 2003 and 2009. FY ice backscatter quickly moves to lower values between September and mid-November. It decreases slightly (sometimes remaining constant) during December and January, and then gradually moves to higher values until mid-March. After March, the backscatter moves to lower values until June. Then it becomes difficult to distinguish ice

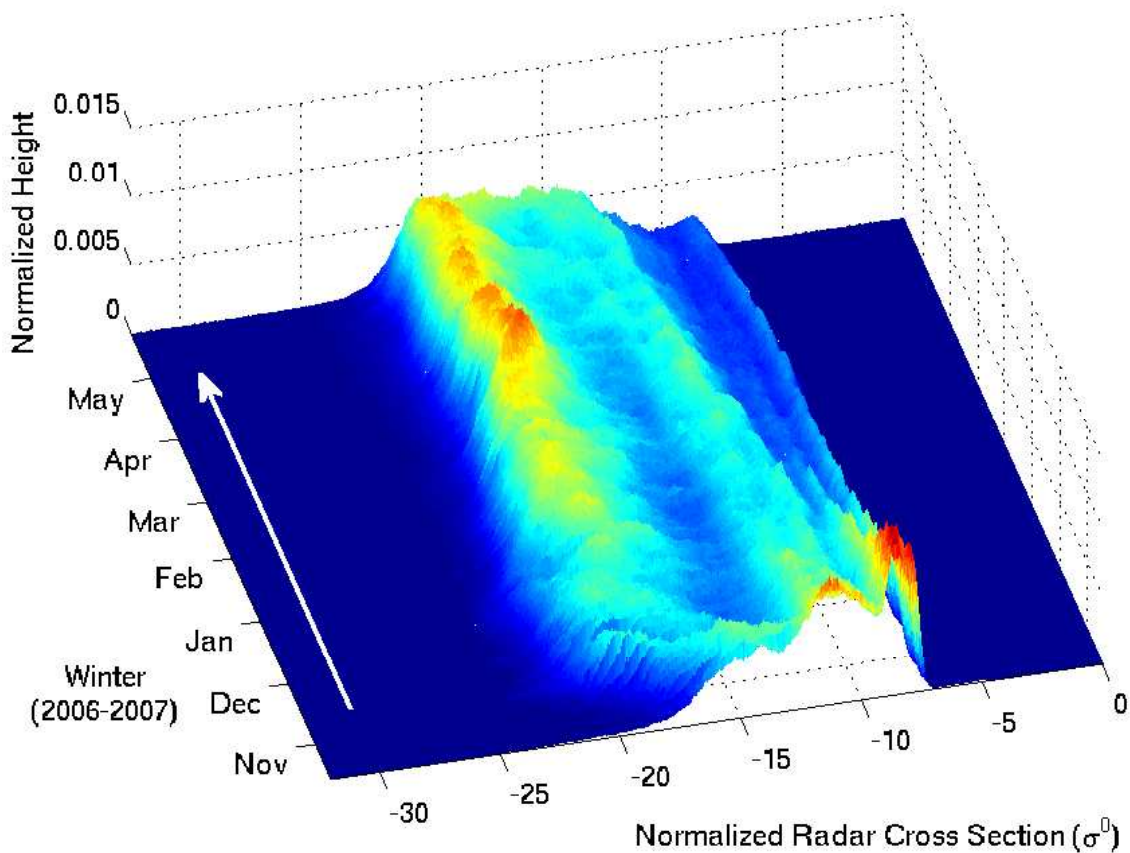


Figure 4.5: Temporal series of histograms of QuikSCAT VV backscatter over sea ice during the 06-07 winter.

type by backscatter until late September due to melting. After September, new ice forms. The variability of the FY ice trend is influenced by several factors. Some of these include new ice formation, brine drainage, ridging and rafting of ice sheets, snow accumulation, ice growth rate (which affects ice salinity), and atmospheric and ocean temperature fluctuations (which affect ice growth).

The backscatter signature of FY ice, in Figure 4.6(a), seems to stabilize mid-November. The high backscatter of FY ice observed prior to mid-November may be partially explained by frost flowers, which are formed by the deposition of ice directly from the vapor phase. Frost flowers have been seen in connection with a sharp increase in backscatter for ice that is 10 to 30 cm thick. The backscatter of this FY ice may be as high as that typically seen for

MY ice. As the ice thickens, the backscatter decreases by roughly 5 to 7 dB and stabilizes to commonly observed values for FY ice [3, 42]. The gradual backscatter increases observed from December to mid-March may be accounted for by brine drainage and roughening of the surface over time. Brine drainage, which begins immediately after ice forms, leads to lower brine volume and consequently lower electromagnetic absorption. The effects of drainage, in combination with increased roughness and snowfall over time, tends to increase scattering [42]. Factors in the subsequent decrease in backscatter may be related to an increase in snow density as discussed later.

4.2.2 Trends in Multi-Year Ice

Referring to Figure 4.6(a), the backscatter signature of MY ice during the 04-05 winter is seasonally dependent. Over the winter, it moves to lower backscatter values with the exception of a pause during January and February. Reduction in MY backscatter might be due in part to snow accumulation and/or increasing snow density. Arctic snow accumulation is greatest in the fall, with little accumulation in December and January, and then gradually increasing accumulation in spring until May [43].

The pattern of snowfall seems to mimic the pattern of decreasing backscatter suggesting a possible connection. Onstott [20] notes that the calculated effect of 10 cm of dry snow over MY ice, with $T_{air} = -20^{\circ}C$ and $T_{ice} = -3.7^{\circ}C$, is a decrease in backscatter by about 0.3 dB. The average snow density in the Arctic has been observed to gradually increase during the winter over MY ice [43]. Under dry snow conditions, snow density, grain size, and stratification are the dominant factors in determining the backscatter coefficient, which is inversely correlated with snow density [44].

In distinguishing ice type by backscatter, there is an implied assumption that backscatter increases as ice ages. In 2004 and later, the mode representing MY ice in Figure 4.9(a) splits into as many as three or more distinguishable modes. An example of these modes is shown in Figure 4.7 for the 07-08 winter. In the following, we show that σ^0 generally increases (to an upper limit) for MY ice after each summer melt.

To study this increase, σ^0 measurements are collocated with the position of buoys deployed in MY ice by the Cold Regions Research and Engineering Laboratory (CRREL).

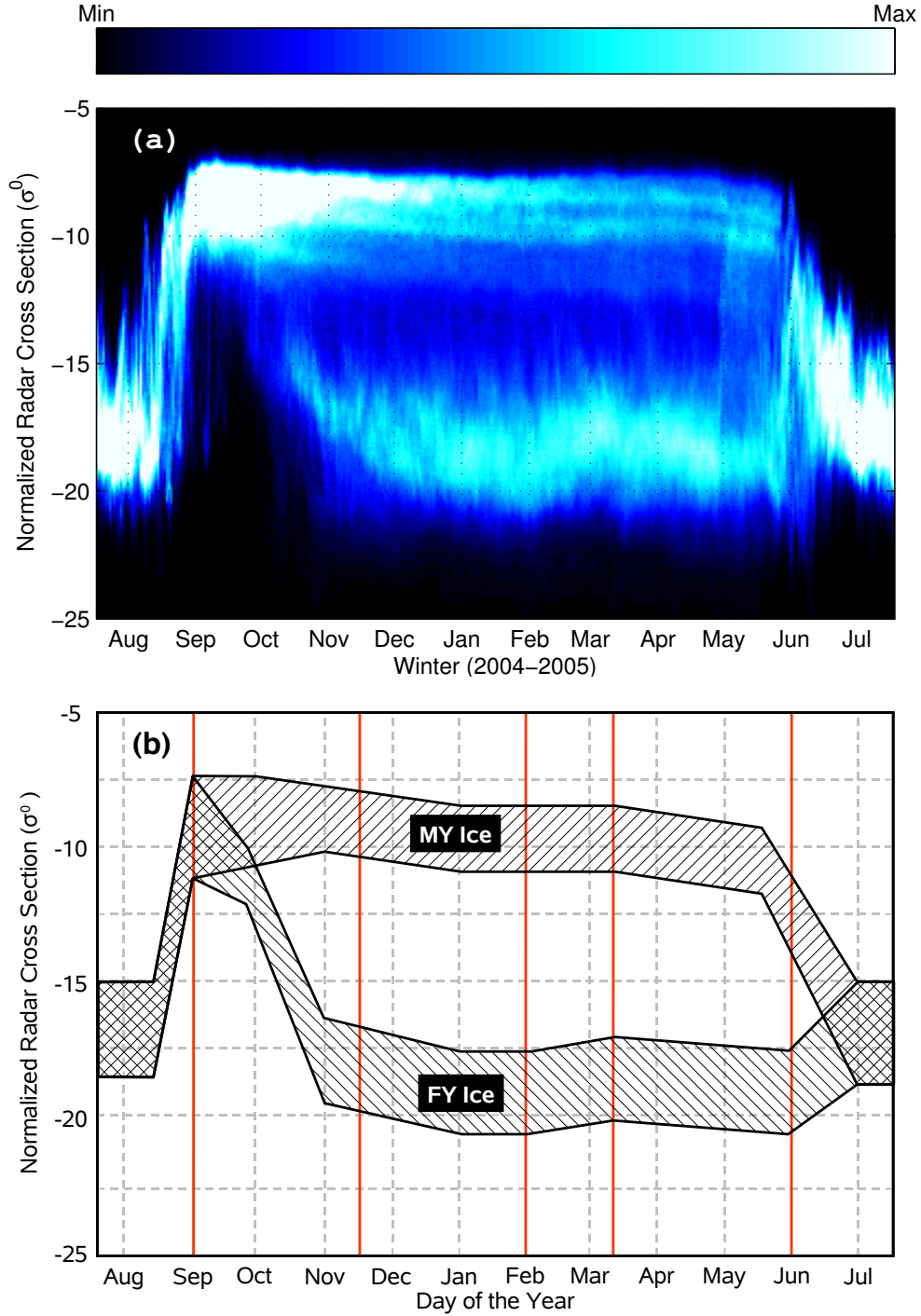


Figure 4.6: Seasonal trends in backscatter over FY and MY ice. (a) shows a time series of histograms of backscatter over Arctic sea ice for the winter of 04-05. (b) shows approximate ranges of backscatter for FY and MY ice for each year between 2003 and 2009. The range of backscatter for each ice type appears to be seasonally dependent.

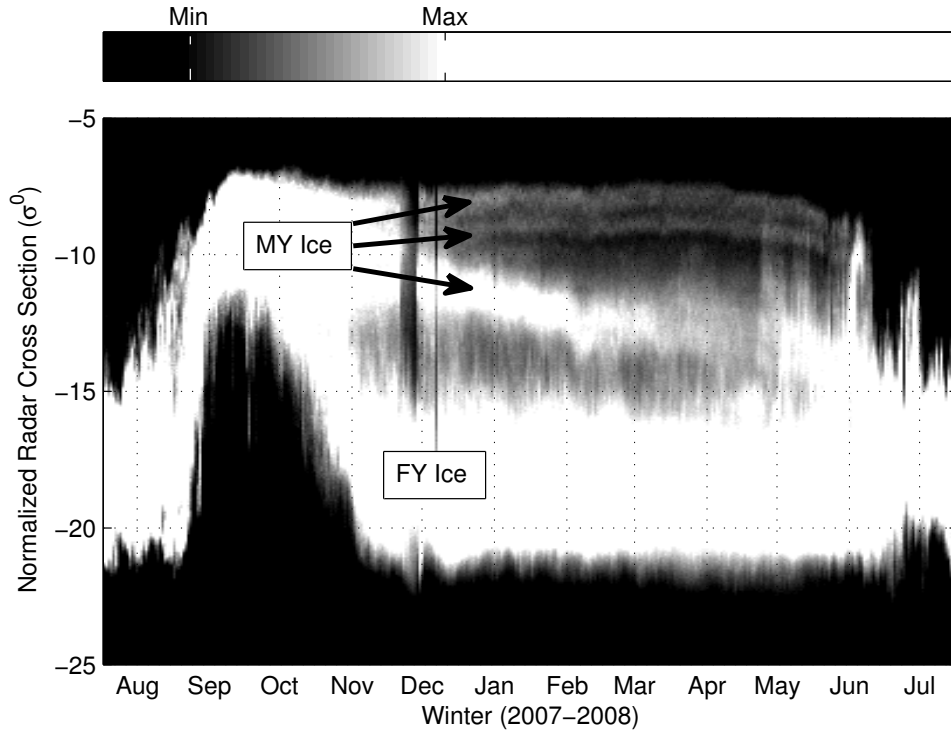


Figure 4.7: Time series of histograms of QuikSCAT VV measurements over sea ice during the 07-08 winter. The gray scale emphasizes that multiple modes are present in the typical range for MY ice.

The buoys allow a parcel of ice to be tracked over time. The implicit assumptions are that buoys are fixed relative to a surrounding parcel of ice, that similar ice characteristics exist within a 5 km radius (QuikSCAT egg resolution), and that temporal disparities of less than one day are acceptable. Tracking the backscatter over an ice parcel provides significant information about the time-varying characteristics of the ice. Of the more than 40 buoys deployed in the Arctic between 2003 and 2009, at least 10 remained active long enough to provide multi-year comparisons.

Typical plots for collocated σ^0 VV measurements for various time periods are shown in Figure 4.8 where corresponding buoy tracks are shown below each plot. Very similar results were obtained using σ^0 HH. CRREL buoy 2005E, which is shown in Figure 4.8(a), was deployed on MY ice at 83 N, 174 W as part of the Healy-Oden Trans-Arctic Expedition (HOTRAX). It traveled toward the north coast of Greenland for two years. Collocated QuikSCAT σ^0 VV backscatter measurements show an increase of about 2 dB between the

winters of 05-06 and 06-07. Buoy 2006C in Figure 4.8(b) was deployed in the Beaufort Sea by the Woods Hole Oceanographic Institution (WHOI). It initially shows a decrease in σ^0 during 2007. However, after the buoy heads out of the Beaufort Gyre, σ^0 increases by about 4 dB between the winters of 07-08 and 08-09. Although very little data is available for the winter of 09-10, there is some indication of an additional increase of about 2 dB.

Buoy 2006F, which was deployed in the Laptev Sea, is shown in Figure 4.8(c). Collocated measurements show an increase of about 4 dB between the end of 2006 and the end of 2007. The trailing off backscatter value at the end of 2007 may be a result of mixed FY and MY ice as the buoy heads out of the Fram Strait. Another possibility may be heavy snowfall causing the ice floe to flood with seawater. This flooding has been previously noted to occur in the Fram Strait[3].

The only case studies of collocated σ^0 and buoy positions not exhibiting an increase in σ^0 are found in the Beaufort Sea. Buoy 2007J, shown in Figure 4.8(d), shows steady σ^0 values for the winter of 07-08, but then decreasing values for the remaining life of the buoy. The observed decrease might be attributed to mixing of FY and MY ice in the Beaufort Gyre, with the possible melting of the ice parcel during the last year of buoy activity. Collocated measurements over three additional buoys (2005B, 2007E, and 2007F) also show decreasing backscatter as each buoy track heads into the Beaufort Gyre. Buoy 2005B survives long enough to exit the gyre and show a post-summer increase in 2007 backscatter in comparison to 2006. Collocated measurements over six additional buoys show post-summer increases in backscatter over the previous year.

While it is difficult to determine the cause of increased backscatter of MY ice in all cases, a possible explanation follows. Microwave scattering results from a combination of surface and volume scatterers. Volume scattering from MY ice is largely a result of air pockets and channels within the ice. During the formation of MY ice in the summer, temperature increases in the upper layers of ice cause brine pockets to enlarge. The enlarged pockets then tend to coalesce and form a vertical network of channels in the ice. When freshwater melt forms on the surface of the ice, it contributes to this network of channels as it percolates through the ice sheet. This process reduces the salinity of the upper 50 to 100 cm of ice to less than 1‰. These changes are a major contributing factor to the large

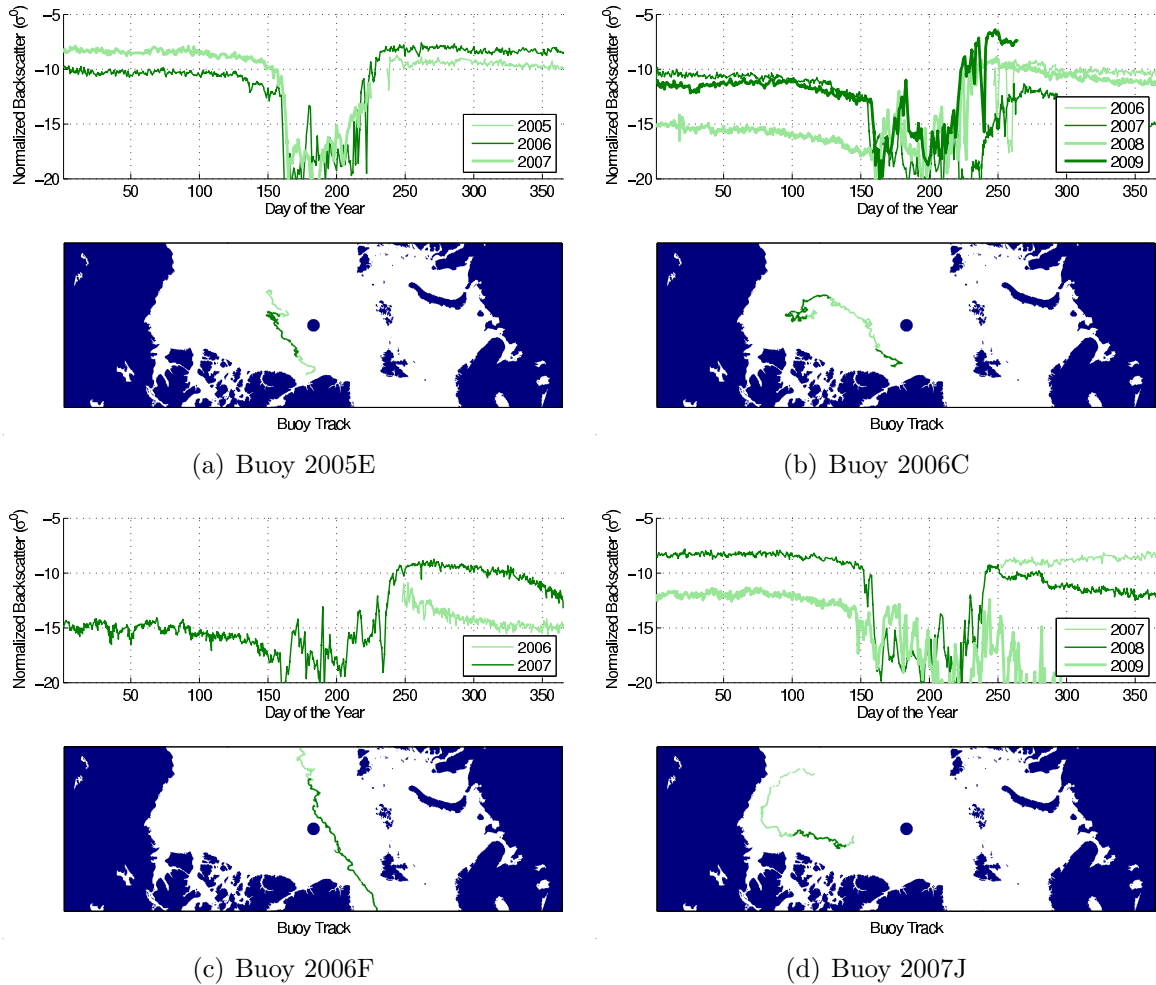


Figure 4.8: Typical results for collocated σ^0 VV measurements and CRREL buoys (above), and buoy positions (below).

backscatter increase of MY ice over FY ice [3]. Percolation of freshwater melt occurs each year, which may cause widening of—or additions to—the vertical network of channels within the ice sheet. Increased porosity of the ice could account for increased volume scattering.

4.2.3 Interannual Trends in Sea Ice Coverage

Interannual trends in sea ice may be observed by analyzing the distribution of σ^0 over a period of several years. Figure 4.9(a) is a plot of daily histograms of normalized backscatter from 2003 to 2009. Figure 4.9(b) is the total area of ice isolated for each day. It shows that the total area of ice under consideration is seasonally consistent. These histograms suggest

a gradual shift in the ice cover from MY to FY ice. The MY ice mode (right) becomes progressively weaker and dispersed during this period, while the FY ice mode (left) becomes progressively stronger. Since Figure 4.9(a) shows that the area of sea ice under consideration does not change significantly from winter to winter, we conclude that MY ice has gradually been replaced by FY ice over this period. We note that there is some indication of a possible rebound of this trend in 2009.

To illustrate the shift in sea ice cover from MY to FY ice, Figure 4.10 shows daily histograms of backscatter during the winters of 02-03 and 08-09. There is a clear increase in FY ice, highlighted by the solid line, as well as a clear decrease in MY ice, highlighted by the dashed line. Selected SIR images from QuikSCAT VV are shown in Figure 4.11 to provide a spatial confirmation of this pattern.

4.3 Conclusion

Interannual trends exist in Ku-band backscatter over FY and MY sea ice. Particularly, MY ice has been observed to increase in backscatter for each melt season it survives. The spatial coverage of MY ice is also observed to decrease significantly between 2003 and 2009. However, in 2009, there is an increase observed in the MY ice cover over the previous year.

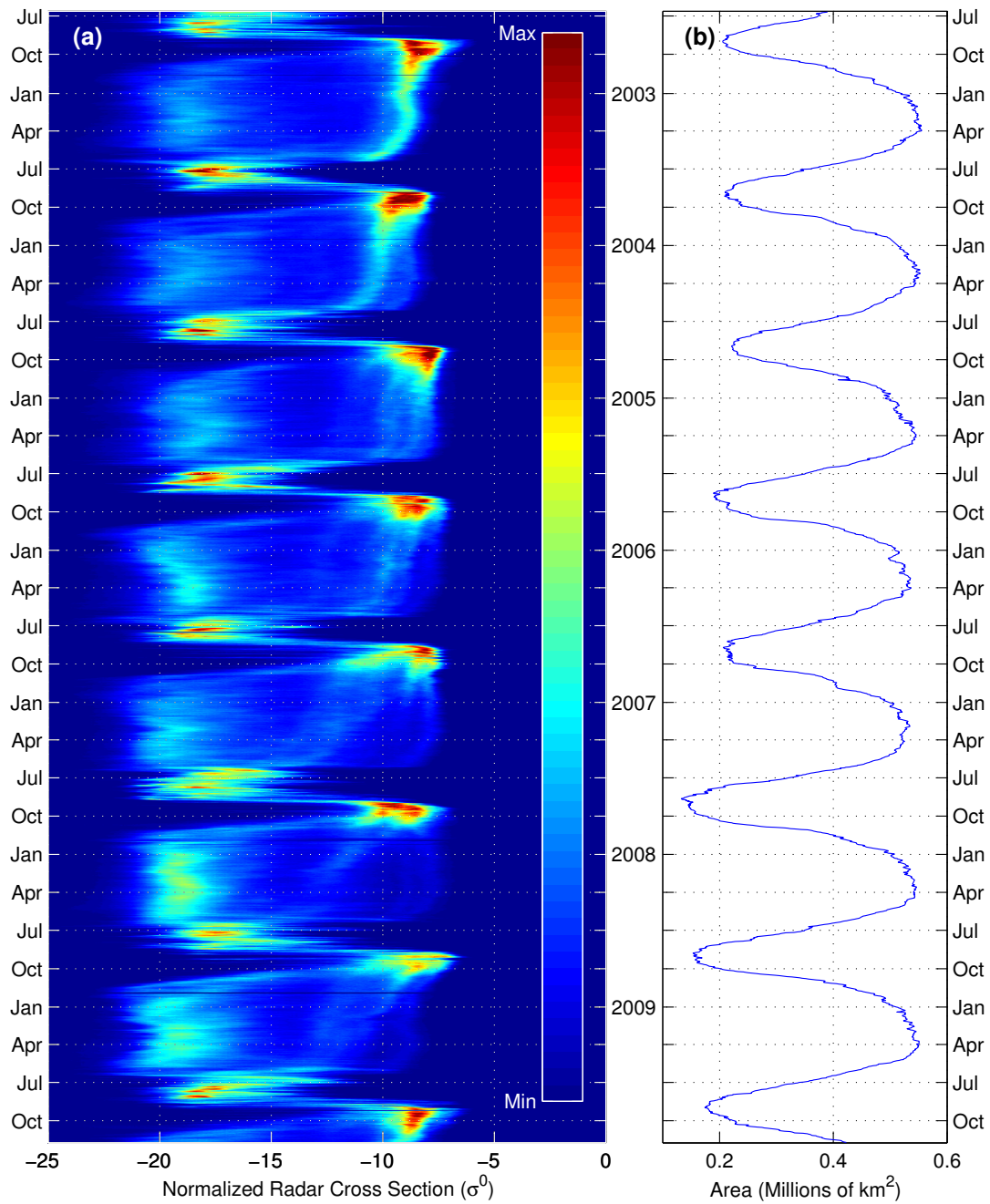


Figure 4.9: (a) Temporal series of histograms of QuikSCAT VV measurements over sea ice, and (b) the total area of ice above the $A_{6,V}$ 220 K threshold for each day.

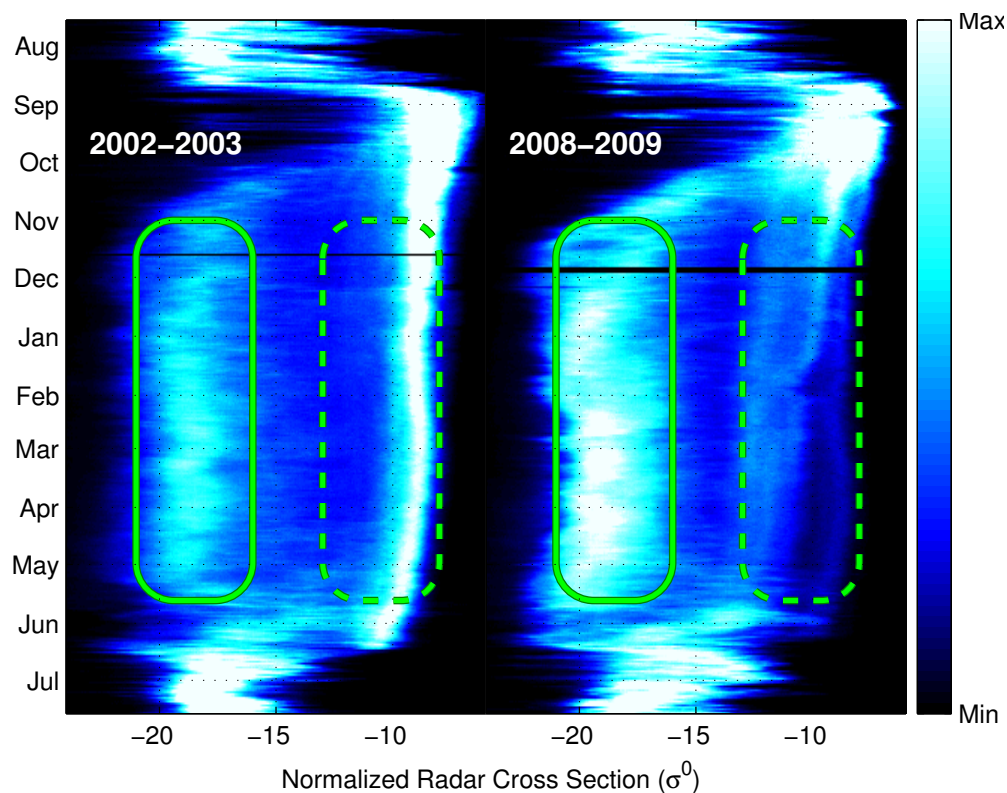


Figure 4.10: A plot of backscatter versus time for two different winters. The winter of 02-03 is shown on the left and 08-09 on the right. The FY ice mode is marked by a solid line, and the MY ice mode by a dashed line for each winter. Note that MY ice distributions are brighter during the winter of 02-03 and FY ice distributions are brighter during the winter of 08-09.

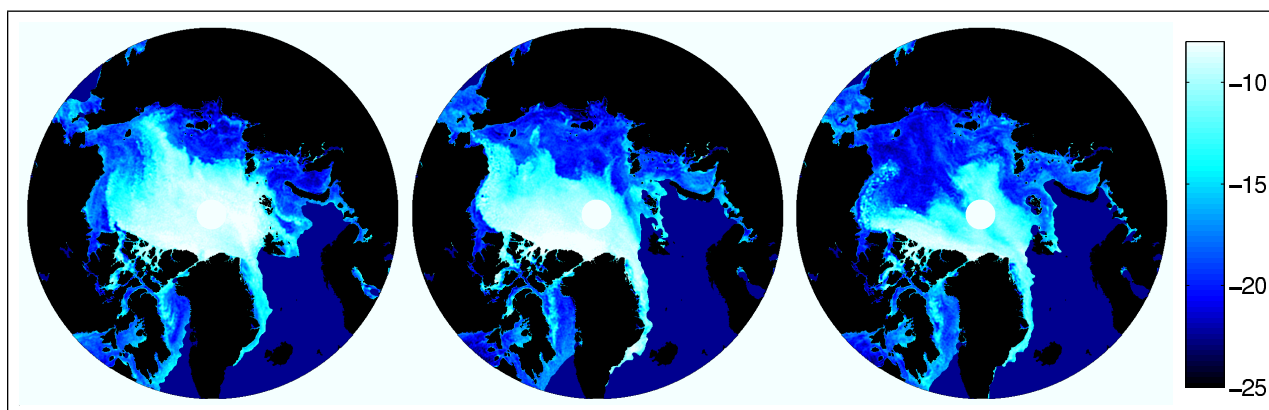


Figure 4.11: Selected QuikSCAT VV (σ^0 in dB) images showing trend in decreasing MY ice from 2003-2009. Images from left to right represent DOY 32, in 2003, 2006, and 2009. Land is shown as black, and ocean is dark blue. Brighter colors correspond to increased backscatter where FY is approximately below -15 dB and MY is above.

Chapter 5

Multi-Year Ice Classification and Validation

5.1 Multi-Year Ice Classification

The trends observed in sea ice backscatter for FY and MY ice appear to be seasonally consistent. Each year, there is a clear separation of FY and MY ice. FY ice has some variations that may be due to snowfall or other weather events, but variations are reasonably small with respect to the larger trends in ice type. For MY ice, the number of observed trends in backscatter depend on the year. The appearance of different signatures from year to year may be explained by the varying spatial coverage of MY ice of different ages. CRREL Buoy 2006F (Figure 4.8(c)), which was deployed in MY ice, gives evidence that MY ice may return backscatter signatures as low as -15 dB.

These observations give rise to a method for FY/MY ice classification using an average of the yearly distributions. Figure 5.1(a) shows histograms of σ^0 VV for an annual period averaged over 7 years (2003 to 2009). The scales of the image are adjusted to show a minimum bin count that exists over most of the winter, which separates distributions associated with FY and MY ice. A threshold model, dependent on the day of the year, is selected by fitting a curve to the minimum of each histogram during the winter. Subjective bounds, which are shown in 5.1(b) are used to approximately isolate the daily minimum. The histogram minimum found between these bounds and the fitted curve are also shown in Figure 5.1(b). A fifth-degree polynomial is fit using a least-squares method. Although seasonal changes in the data are naturally periodic, a polynomial fit locally approximates periodic data and can be fit to seasonal changes.

A limitation of this classification method is that MY ice can sometimes look like FY ice. Comiso suggests that ice floes near the MIZ, that survive the summer melt often have passive microwave signatures similar to FY or intermediate ice later in the winter. He

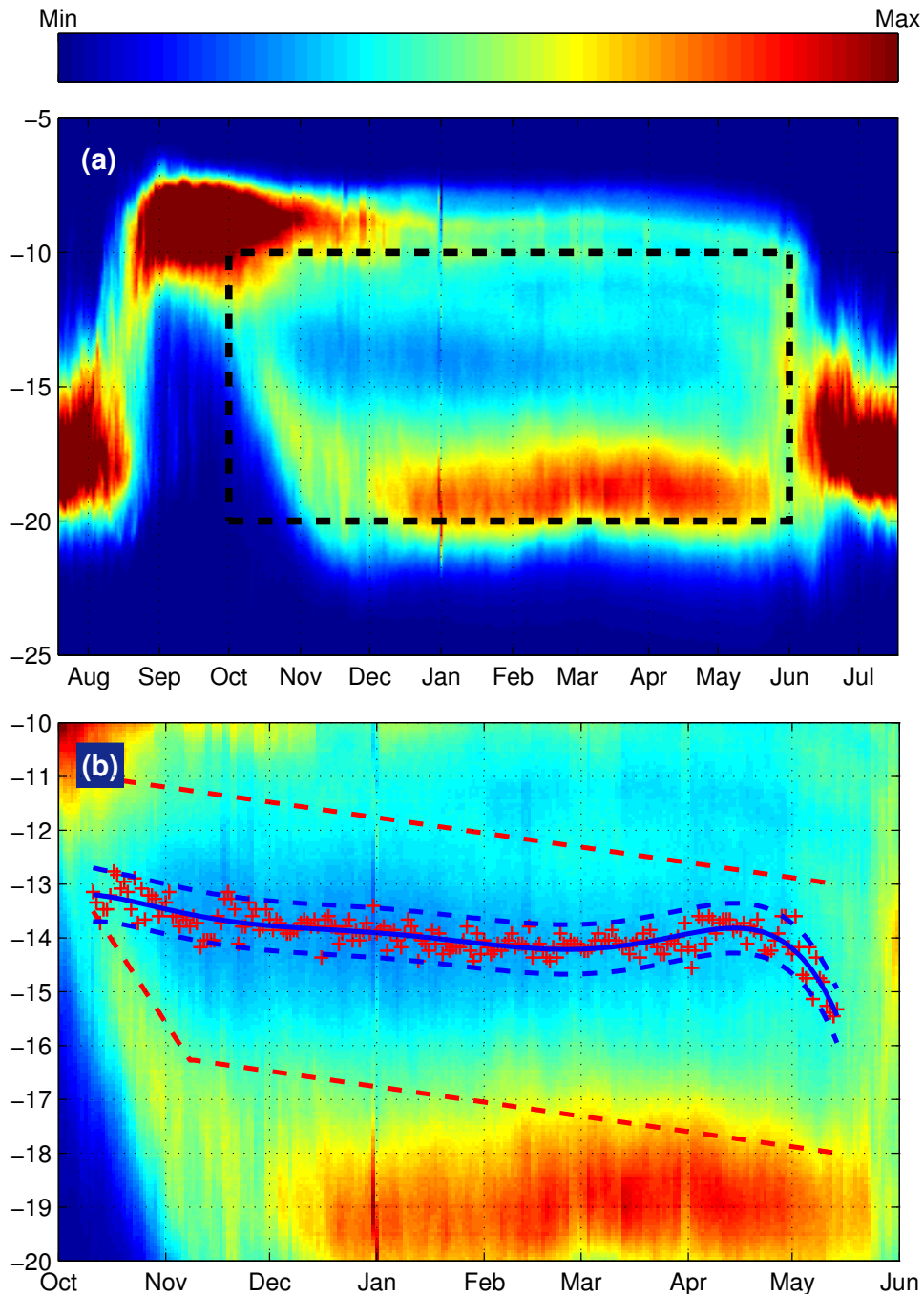


Figure 5.1: (a) An annual time series of daily histograms averaged over 7 years (2003 to 2009). The dashed box represents a subset shown in (b). (b) The classification threshold on QuikSCAT backscatter distributions. Shown are bounds set to select the minimum (dashed straight lines), the minimum found for each day of the year (+), and a curve fitted to the results (solid curve) with 95% confidence intervals (dashed curves).

suggests that this is due to the intrusion of seawater into the snow-ice interface during the summer [45]. This intrusion affects active microwave signatures due to the salty ocean water entering the porous upper layers of the ice. Flooding of MY ice has been observed in the Fram Strait by Tucker *et al.*. They found that surface flooding was observed on about 30% of sampled ice flows [3]. In some instances, FY ice may also look like MY ice if it has undergone significant rafting and ridging and/or brine exclusion.

5.2 Validation

Ice charts from the Canadian Ice Service (CIS) are used to validate the classification of FY and MY ice. These charts are based on an analysis and integration of several data sources, including weather and oceanographic information; in situ observations from land, ship and aircraft; airborne radar; and satellite imagery. We note that validation using these charts may not be completely independent due to the use of satellite data. Regional ice charts provide an analysis of ice conditions for a given region and date, where data up to three days prior is used to determine ice concentration, stage of development, and ice form, following World Meteorological Organization terminology. Ice charts have been available on a weekly (sometimes bi-weekly) basis since 2006. For validation, the most useful regions are the Western Arctic and Eastern Arctic shown in Figure 5.2. These regions are commonly covered by FY and MY ice. The regions themselves are divided up by CIS analysts into approximately homogeneous subregions and assigned a total ice concentration. The three most prominent ice types within the subregion are recorded with their partial concentration, stage of development and thickness, and form or floe size. The sum of the partial ice concentrations is always less than or equal to the total ice concentration for the subregion. The data for each subregion is contained in an oval chart typically referred to as an egg code.

In order to compare CIS ice charts with FY and MY ice classifications derived from QuikSCAT backscatter, ice chart stages surviving at least one melt season (Old Ice, Second-Year Ice, and Multi-Year Ice) are grouped as MY ice and all other ice types are grouped as FY ice. For the purpose of comparison, the ice stage within a subregion with the highest partial ice concentration is assumed to represent the whole subregion. In order to reduce

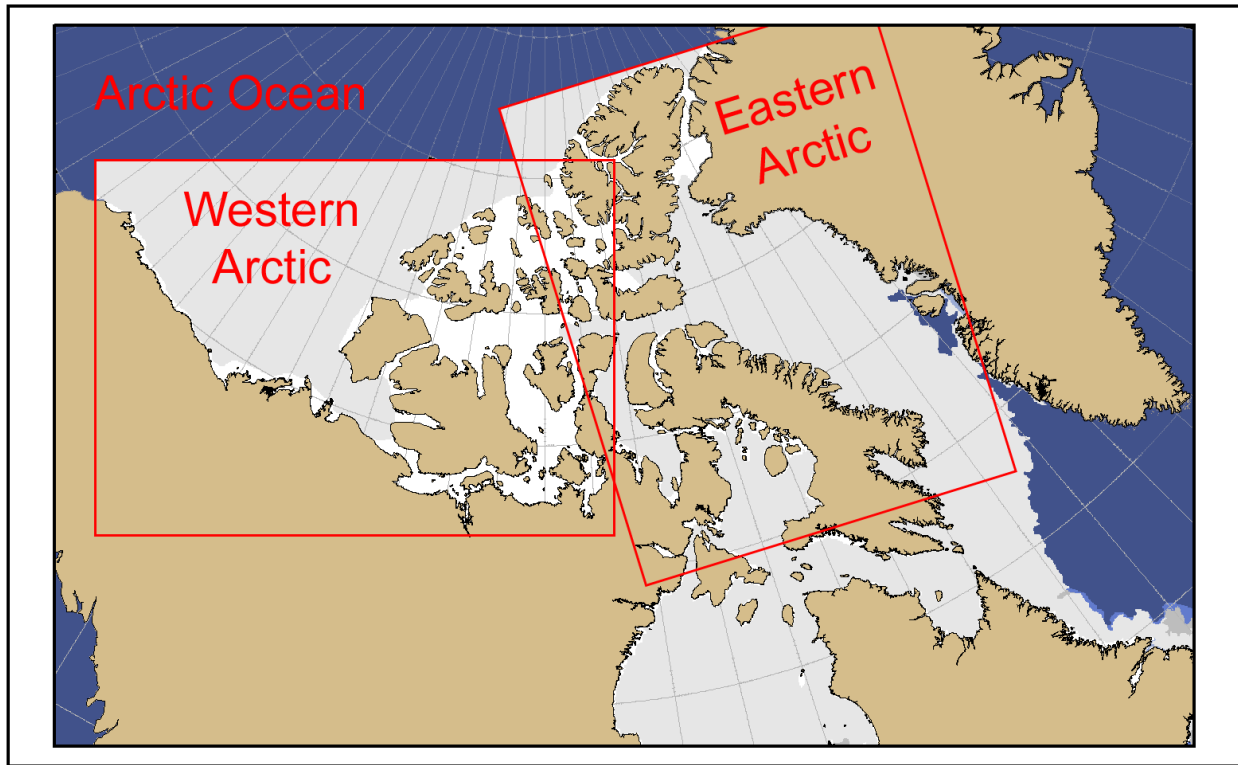


Figure 5.2: Canadian Ice Service Chart Regions (Modified from [46]).

error that may be introduced by this assumption, only subregions in which the highest partial ice concentration is 70% or greater are considered. The next highest partial ice concentration for these subregions is less than 30% by definition and is assumed to make little contribution. When a range of partial ice concentrations is specified in the CIS ice charts, the average is used. For example, for the partial ice concentration of 60 to 80%, a value of 70% is assumed. Each ice chart region is formatted as a shape file in SIGRID-3 format with the latitude and longitude specified for the vertices of each shape. Figure 5.3 shows the Western Arctic CIS ice chart region collocated with QuikSCAT VV on DOY 42, 2008. In Figure 5.3(a), subregions within the ice chart are colored by the percent ice concentration of the ice stage with the highest concentration. Figure 5.3(b) shows ice stages grouped as FY or MY ice overlaid on a QuikSCAT SIR image. The CIS ice chart appears to be a natural extension of the QuikSCAT SIR image.

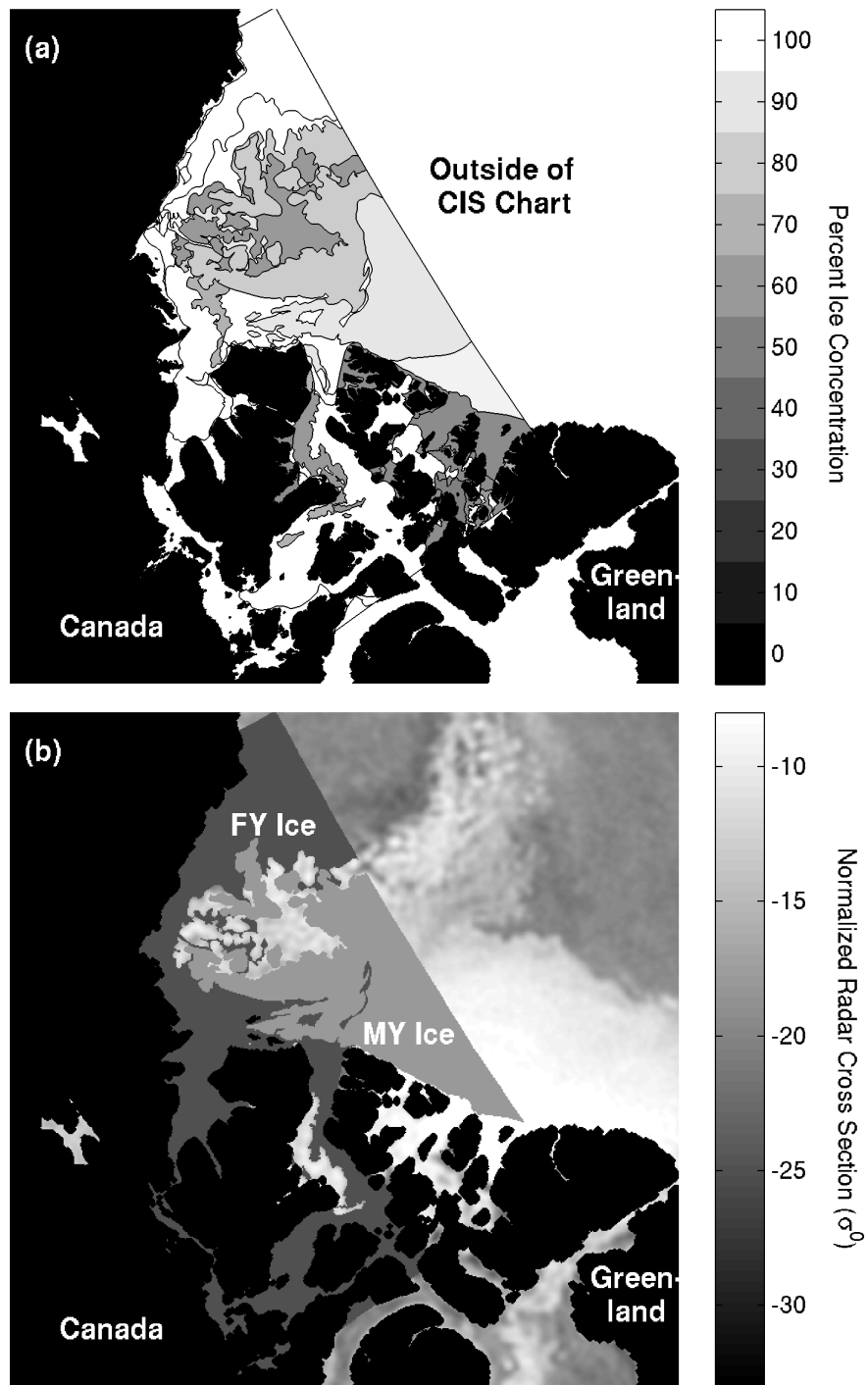


Figure 5.3: Collocated CIS Western Arctic ice chart and QuikSCAT SIR image on DOY 42, 2008. Land is black. (a) shows the percent ice concentration for the highest ice stage concentrations for each ice chart subregion. (b) shows ice stage concentrations above 70% grouped as FY or MY ice overlaid on a QuikSCAT SIR image (σ^0 in dB).

For the winters (November through April) of 06-07, 07-08, and the end of 2008, the total average error for the Western Arctic and Eastern Arctic regions is $5.84 \pm 3.52\%$ error. This classification is biased toward MY ice, where classification of FY ice as MY ice accounts for 3.83% of the average error. For illustration, the classification error for 2008 is shown in Figure 5.4 for the Western Arctic (a) and Eastern Arctic (b) regions. We note that there is a slight performance difference with respect to error between the Western Arctic and Eastern Arctic regions. With a fixed threshold of -14.5 dB on σ^0 , as in [14], the total average error is $7.16 \pm 3.75\%$ error. The fixed classification is also biased toward MY ice, where classification of FY ice as MY accounts for 6.01% of the average error. We conclude that for the validation regions, a seasonally varying classification threshold performs better than using a fixed threshold of -14.5 dB and has less bias toward MY ice. Further validation using CIS ice charts is limited by chart availability.

5.3 Discussion of Results

Results from ice classification using QuikSCAT are shown in Figure 5.5 for DOY 32, 2003 through 2009. These typical results reveal the MY ice loss trend previously noted from the temporal trends in Figure 4.9. The loss of MY ice can be accounted for by multiple events. These include surface melt due to air temperature and solar heat, bottom melt due to warm ocean water, and ice advection. Particularly, ice advection through the Fram Strait has been noted as a source of MY ice loss in multiple studies ([47, 48] for example). The evidence presented in this paper indicates that while the total area of highly consolidated ice has fluctuated to a small degree between 2002 and 2009, there has been a shift from MY ice to FY ice. This shift is evident using both active and passive microwave sensors. Although this trend is consistent over the selected years, it appears that in 2009 there may be a small increase in MY ice.

5.4 Conclusion

Classifying FY and MY sea ice over the winter using a Ku-band scatterometer can be accurately accomplished using a seasonally dependent threshold to separate ice types. The results are consistent with CIS ice charts. An average ice classification error of 5.84%

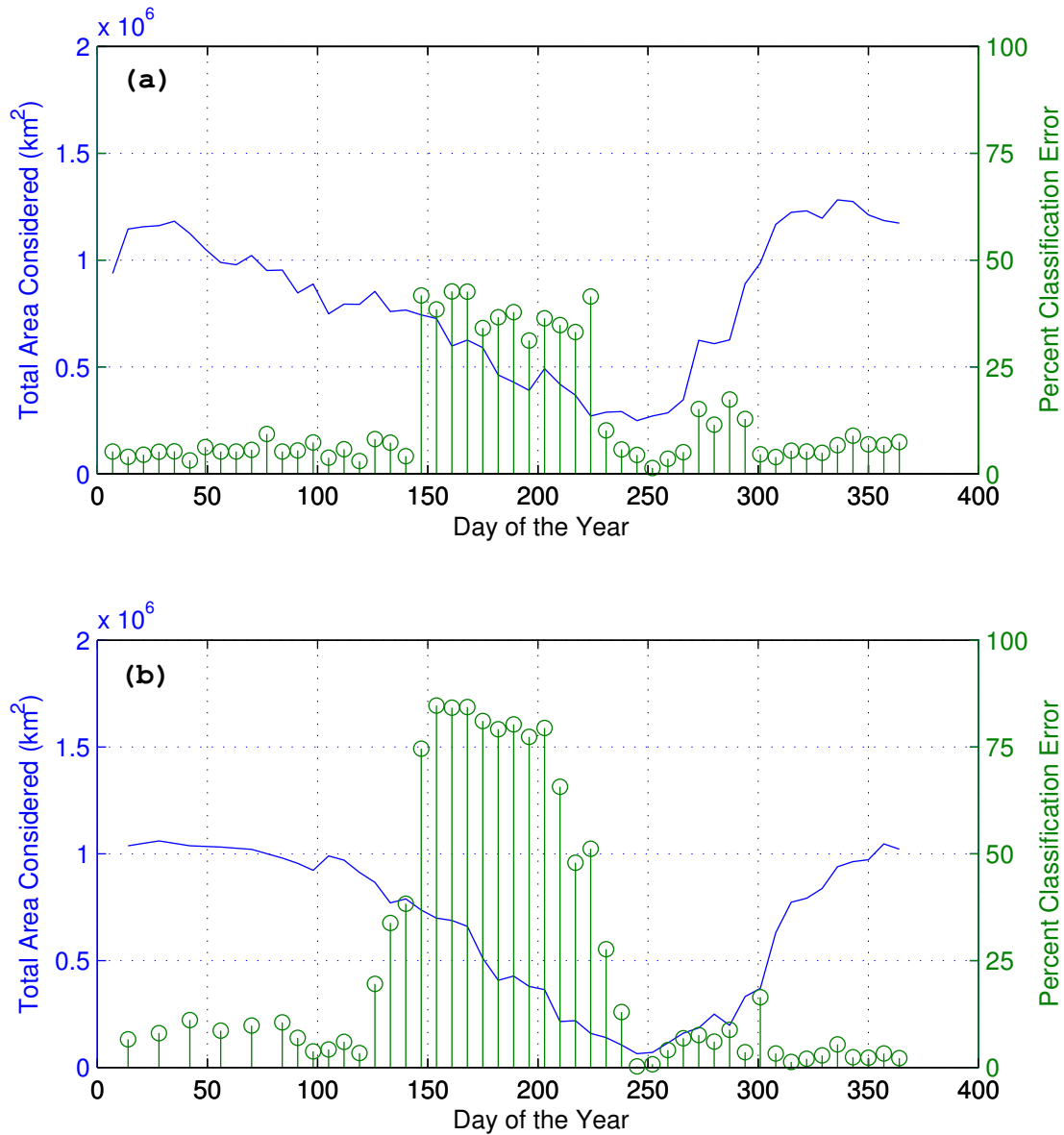


Figure 5.4: Classification error of QuikSCAT-derived FY/MY ice using CIS ice charts. The error represents the percentage of ice cover misclassified using QuikSCAT σ^0 for the (a) Western Arctic and (b) Eastern Arctic regions. The total area of ice considered (solid line) and the error for each day (stem plot) are shown.

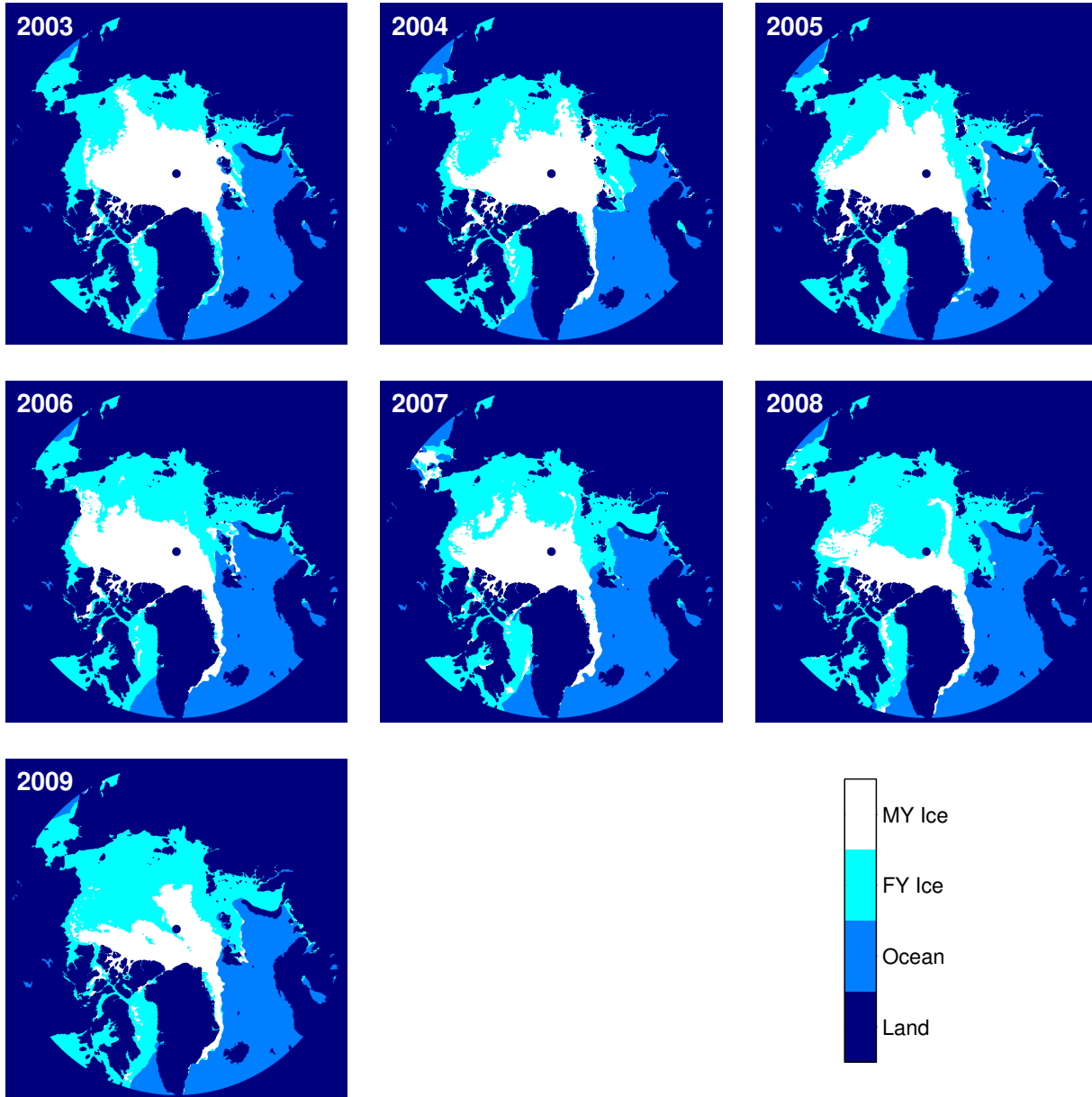


Figure 5.5: Ice classification using QuikSCAT for DOY 32, 2003 through 2009. Note the trend in decreasing spatial coverage of MY sea ice.

is observed for Western and Eastern Arctic regions during the winter (November through April) compared to an average error of 7.16% when using the fixed threshold found in [14]. This seasonal model makes no attempt to classify ice during the summer.

Chapter 6

Conclusion

Arctic sea ice is an important component of the polar environment. Chapter 1 describes some of the influential characteristics of sea ice and the impact of its growth or loss. Many methods are used to measure and characterize sea ice. Satellite microwave sensing of the Arctic provides good temporal and spatial resolution independent of season or solar illumination. The past decade of sea ice observation is particularly interesting because of an observed reduction in sea ice coverage as indicated by a number of studies.

Chapter 2 provides a detailed description of the formation of sea ice for a calm water scenario. While many other scenarios are possible, this scenario describes several fundamental components of sea ice growth. Understanding sea ice growth is valuable for the interpretation of microwave measurements. Chapter 2 also provides a broad overview and history of satellite microwave sensing using active and passive sensors. The fundamental principles of radiometry and scatterometry are discussed along with an application to the NASA Team algorithm.

Chapter 3 describes the methods used to investigate sea ice. Products derived from collocated QuikSCAT and AMSR-E measurements show promise in the classification of sea ice. In particular, sea ice classification is attempted using two different approaches to data clustering.

In Chapter 4, the Arctic is initially classified as sea ice and open water using measurements from the 6 GHz channel of AMSR-E. Temporal series of histograms over sea ice provide an insightful and useful perspective on seasonal changes. Interannual trends are shown to exist in Ku-band backscatter over FY and MY sea ice. Particularly, MY sea ice is observed to increase in backscatter for each melt season it survives. This is verified by tracking backscatter over Arctic buoys secured to MY ice.

Through an investigation of the microwave signatures of Arctic sea ice, a new method for the classification of MY sea ice is developed in Chapter 5. This demonstrates the potential of scatterometry in sea ice classification. Classifying FY and MY sea ice over the winter using a Ku-band scatterometer can be accurately accomplished using a seasonally dependent threshold to separate ice types. The results are consistent with CIS ice charts.

6.1 Contributions

The research presented in this thesis contributes to the body of published work on the remote sensing of Arctic sea ice. Essential results in Chapters 4 and 5 have been submitted for publication. The contributions of this thesis are summarized in the following sections.

6.1.1 Automated Data Clustering

Automated data clustering can be accomplished by a number of algorithms with differing degrees of success and computational load. The OPTICS (Ordering Points To Identify the Clustering Structure) algorithm [39] claims to be an efficient and effective tool for this purpose and was selected and implemented as a MATLAB MEX file. The algorithm was used successfully to search for clustering of sea ice signatures in the multitude of available active and passive microwave data sets.

6.1.2 New Classification Method

Chapter 4 describes seasonal trends in Ku-band backscatter over FY and MY ice. Based on an average of these trends, a new MY sea ice classification method is developed and described in Chapter 5. This classification method provides independent verification of MY sea ice loss over the past decade.

6.1.3 Documented Sea Ice Change

Loss in MY sea ice coverage is observed spatially and in the proportion of FY to MY sea ice measurements from season to season using QuikSCAT. The year-to-year evolution of backscatter over MY sea ice is also observed by collocating σ^0 and CRREL buoy positions. This is a new method for investigating the evolution of MY sea ice signatures.

6.2 Future Research

While pursuing the research presented in this thesis, I identified several areas for possible future research. These areas are discussed in the following sections.

6.2.1 Backscatter Derived Sea Ice Age

MY Arctic sea ice is found in this research to reflect backscatter indicative of ice age. Further study of the relationship between σ^0 and ice age may yield a model to estimate ice age based on backscatter measurements.

6.2.2 Optimal Sea Ice Classification

The sea ice classification method described in Chapter 5 is derived using a minimum histogram value between modes of FY and MY ice for each day of the winter. This is a sub-optimal approach because the minimum histogram bin does not necessarily represent an optimal threshold. In further work, an optimal threshold may be selected by assuming a probability model from which probabilities of detection and false alarm can be derived. This may be done in different ways. The model may be allowed to change with a weighting on the current year or may assume that sea ice signatures are fixed from year to year.

6.2.3 Joint Active and Passive Microwave Sea Ice Classification

Chapter 3 cites several studies indicating the benefit of using both active and passive microwave sensors for sea ice classification. In the new classification method developed in this thesis, only active data is used. An investigation of the seasonal trends in passive microwave data may provide a complimentary model.

The clustering methods described in Chapter 3 may be used with active and passive data. Further study of automated clustering for sea ice classification using active and passive sensors may be useful.

6.2.4 Active Sea Ice Classification Using C-Band

Many of the results in this thesis may potentially be extended using the long history of available scatterometer data. Particularly, C-band data sets are available from the Euro-

pean Remote-Sensing Satellites (ERS 1 and 2) and the Advanced Scatterometer (ASCAT) launched by the European Space Agency.

6.2.5 Additional Validation

Additional validation of the sea ice classification method presented in this thesis is warranted. Validation techniques may include comparisons with Arctic SAR imagery and/or optical imagery. Although not presented in this thesis, limited efforts were made to validate against laser altimeter measurements, relying on the relationship between ice age and ice thickness. Further work in this direction, such as comparisons with submarine ice draft profiles, may yield useful results.

Bibliography

- [1] F. Carsey, *Microwave remote sensing of sea ice*. American Geophysical Union, 1992. 1
- [2] F. Fetterer, K. Knowles, W. Meier, and M. Savoie. (2009) Sea ice index. National Snow and Ice Data Center, Boulder, CO. Digital media. [Online]. Available: http://nsidc.org/data/seaice_index/ 1
- [3] W. Tucker, D. Perovich, A. Gow, W. Weeks, and M. Drinkwater, *Microwave remote sensing of sea ice*. American Geophysical Union, 1992, ch. Physical Properties of Sea Ice Relevant to Remote Sensing. xiii, 1, 9, 10, 49, 52, 53, 59
- [4] N. Short. (2010, April) Remote sensing tutorial. [Online]. Available: <http://rst.gsfc.nasa.gov/> 1
- [5] I. Rigor and J. Wallace, “Variations in the age of Arctic sea-ice and summer sea-ice extent,” *Geophysical Research Letter*, vol. 31, no. 9, 2004. 2
- [6] D. Cavalieri, P. Gloersen, and W. Campbell, “Determination of sea ice parameters with the Nimbus 7 SMMR,” *Journal of Geophysical Research*, vol. 89, no. D4, pp. 5355–5369, 1984. 3, 12, 17
- [7] J. Comiso, “Characteristics of Arctic winter sea ice from satellite multispectral microwave observations,” *Journal of Geophysical Research*, vol. 91, no. C1, pp. 975–994, 1986. 3, 4
- [8] —, “SSM/I concentration using the bootstrap algorithm. NASA Report 1380,” *Annals of Glaciology*, vol. 34, pp. 441–446, 1995. 3
- [9] L. Kaleschke, G. Heygster, C. Lüpkes, A. Bochert, J. Hartmann, J. Haarpaintner, and T. Vihma, “SSM/I sea ice remote sensing for mesoscale ocean-atmosphere interaction analysis: Ice and icebergs,” *Canadian Journal of Remote Sensing*, vol. 27, no. 5, pp. 526–537, 2001. 3
- [10] C. Swift, L. Fedor, and R. Ramseier, “An algorithm to measure sea ice concentration with microwave radiometers,” *Journal of Geophysical Research*, vol. 90, no. C1, pp. 1087–1099, 1985. 3
- [11] Q. Remund and D. Long, “Sea ice extent mapping using Ku-band scatterometer data,” *Journal of Geophysical Research*, vol. 104, no. C5, p. 11515, 1999. 3
- [12] R. Ezraty and A. Cavanié, “Intercomparison of backscatter maps over Arctic sea ice from NSCAT and the ERS scatterometer,” *Journal of Geophysical Research*, vol. 104, no. C5, p. 11471, 1999. 3, 4

- [13] G. Belchansky and D. Douglas, "Classification methods for monitoring Arctic sea ice using OKEAN passive/active two-channel microwave data," *Remote Sensing of Environment*, vol. 73, no. 3, pp. 307–322, 2000. 3
- [14] R. Kwok, "Annual cycles of multiyear sea ice coverage of the Arctic Ocean: 1999–2003," *Journal of Geophysical Research*, vol. 109, p. C11004, 2004. 3, 4, 62, 65
- [15] R. Kwok, G. Cunningham, M. Wensnahan, I. Rigor, H. Zwally, and D. Yi, "Thinning and volume loss of the Arctic Ocean sea ice cover: 2003–2008," *Journal of Geophysical Research*, vol. 114, no. C7, 2009. 3, 5
- [16] F. Carsey, "Arctic sea ice distribution at end of summer 1973–1976 from satellite microwave data," *Journal of Geophysical Research*, vol. 87, no. C8, pp. 5809–5835, 1982. 4
- [17] D. Thomas and D. Rothrock, "The Arctic Ocean ice balance: A Kalman smoother estimate," *Journal of geophysical research*, vol. 98, no. C6, pp. 10 053–10, 1993. 4
- [18] R. Kwok, G. Cunningham, and S. Yueh, "Area balance of the Arctic Ocean perennial ice zone - October 1996 to April 1997," *Journal of Geophysical Research*, vol. 104, p. 25, 1999. 4
- [19] A. Swan and D. Long, "Multi-year arctic sea ice classification using quikscat," *IEEE Trans. Geosci. Remote Sens.*, vol. in review, 2011. 6
- [20] R. G. Onstott, *Microwave remote sensing of sea ice*. American Geophysical Union, 1992, ch. SAR and Scatterometer Signatures of Sea Ice. xiii, 11, 14, 47, 49
- [21] F. Ulaby, R. Moore, and A. Fung, *Microwave remote sensing: active and passive*. Artech House, Norwood, MA, 1981, vol. 1. 12, 24
- [22] T. Wilhelm, "The electrically scanning microwave radiometer (ESMR) experiment," *The Nimbus-5 user's guide*, pp. 59–104, 1972. 12
- [23] P. Gloersen and D. Cavalieri, "Reduction of weather effects in the calculation of sea ice concentration from microwave radiances," *Journal of Geophysical Research*, vol. 91, pp. 3913–3919, 1986. 12, 30
- [24] D. Cavalieri, K. St Germain, and C. Swift, "Reduction of weather effects in the calculation of sea-ice concentration with the DMSP SSM/I," *Journal of Glaciology*, vol. 41, no. 139, pp. 455–464, 1995. 12, 19, 44
- [25] D. Cavalieri. (2003, May) NASA team sea ice algorithm. [Online]. Available: <http://nsidc.org/data/docs/daac/nasateam/> 13, 16, 18, 19, 27, 44
- [26] T. Kawanishi, T. Sezai, Y. Ito, K. Imaoka, T. Takeshima, Y. Ishido, A. Shibata, M. Miura, H. Inahata, and R. Spencer, "The advanced microwave scanning radiometer for the earth observing system (AMSR-E), NASDA's contribution to the EOS for global energy and water cycle studies," *IEEE Trans. Geosci. Remote Sens.*, vol. 41, no. 2, pp. 184–194, 2003. 13

- [27] F. Ulaby, R. Moore, and A. Fung, *Microwave remote sensing: active and passive*. Artech House, Norwood, MA, 1986, vol. 3. xiii, 13, 26
- [28] J. Huddleston and M. Spencer, “The QuikSCAT wind scatterometer mission,” in *2001 IEEE Aerospace Conference, Big Sky, Montana, USA*, 2000. 15
- [29] M. Spencer, C. Wu, and D. Long, “Improved resolution backscatter measurements with the SeaWinds pencil-beam scatterometer,” *IEEE Trans. Geosci. Remote Sens.*, vol. 38, no. 1, pp. 89–104, 2000. xiii, 15
- [30] D. Early and D. Long, “Image reconstruction and enhanced resolution imaging from irregular samples,” *IEEE Trans. Geosci. Remote Sens.*, vol. 39, no. 2, pp. 291–302, 2001. 16
- [31] D. Long and D. Daum, “Spatial resolution enhancement of SSM/I data,” *IEEE Trans. Geosci. Remote Sens.*, vol. 36, no. 2, pp. 407–417, 1998. 16
- [32] The MathWorks, Inc. (2011, May) Dilate image. [Online]. Available: <http://www.mathworks.com/help/toolbox/images/ref/imdilate.html> 22
- [33] P. Yu, D. Clausi, and S. Howell, “Fusing AMSR-E and QuikSCAT imagery for improved sea ice recognition,” *IEEE Trans. Geosci. Remote Sens.*, vol. 47, no. 7, pp. 1980–1989, 2009. 22
- [34] N. Walker, K. Partington, M. Van Woert, and T. Street, “Arctic sea ice type and concentration mapping using passive and active microwave sensors,” *IEEE Trans. Geosci. Remote Sens.*, vol. 44, no. 12, pp. 3574–3584, 2006. 22
- [35] M. Drinkwater, J. Crawford, and D. Cavalieri, “Multi-frequency, multi-polarization SAR and radiometer sea ice classification,” in *IGARSS’91*, 1991, pp. 107–111. 22
- [36] W. Tucker, T. Grenfell, R. Onstott, D. Perovich, A. Gow, R. Snuchman, and L. Sutherland, “Microwave and physical properties of sea ice in the winter marginal ice zone,” *Journal of Geophysical Research*, vol. 96, no. C3, pp. 4573–4587, 1991. 22
- [37] T. Grenfell, D. Cavalieri, J. Comiso, M. Drinkwater, R. Onstott, I. Rubinstein, K. Steffen, and D. Winebrenner, *Microwave remote sensing of sea ice*. American Geophysical Union: Washington, DC, 1992, ch. Considerations for microwave remote sensing of thin sea ice, pp. 291–301. 22
- [38] F. Ulaby, R. Moore, and A. Fung, *Microwave remote sensing: active and passive*. Artech House, Norwood, MA, 1981, vol. 2. 24
- [39] M. Ankerst, M. Breunig, H. Kriegel, and J. Sander, “OPTICS: Ordering points to identify the clustering structure,” *ACM SIGMOD Record*, vol. 28, no. 2, p. 60, 1999. 34, 68

- [40] D. Eppler, L. Farmer, A. Lohanick, M. Anderson, D. Cavalieri, J. Comiso, P. Glorsen, C. Garrity, T. Grenfell, M. Hallikainen, J. Maslanik, C. Matzler, R. Melloh, I. Rubinstein, and C. Swift, *Microwave remote sensing of sea ice*. American Geophysical Union, 1992, ch. Passive Microwave Signatures of Sea Ice. 43
- [41] S. Nghiem, Y. Chao, G. Neumann, P. Li, D. Perovich, T. Street, and P. Clemente-Colón, “Depletion of perennial sea ice in the East Arctic Ocean,” *Geophysical Research Letters*, vol. 33, no. 17, p. L17501, 2006. 46
- [42] M. Hallikainen and D. P. Winebrenner, *Microwave remote sensing of sea ice*. American Geophysical Union, 1992, ch. The Physical Basis for Sea Ice Remote Sensing. 49
- [43] S. Warren, I. Rigor, N. Untersteiner, V. Radionov, N. Bryazgin, Y. Aleksandrov, and R. Colony, “Snow depth on Arctic sea ice,” *Journal of Climate*, vol. 12, no. 6, pp. 1814–1829, 1999. 49
- [44] C. Duguay and A. Pietroniro, *Remote sensing in northern hydrology: measuring environmental change*. American Geophysical Union, 2005. 49
- [45] J. Comiso, “Arctic multiyear ice classification and summer ice cover using passive microwave satellite data,” *Journal of Geophysical Research*, vol. 95, no. C8, p. 13411, 1990. 59
- [46] Canadian Ice Service. Environment Canada. [Online]. Available: <http://www.ec.gc.ca/glaces-ice/> xvi, 60
- [47] R. Kwok, G. Cunningham, and S. Pang, “Fram Strait sea ice outflow,” *Journal of Geophysical Research*, vol. 109, c09009, 2004. 62
- [48] I. Rigor, J. Wallace, and R. Colony, “Response of sea ice to the Arctic Oscillation,” *Journal of Climate*, vol. 15, no. 18, pp. 2648–2663, 2002. 62